First results from the retrieved column O/N2 ratio from the Ionospheric Connection Explorer (ICON): Longitudinal structures induced by nonmigrating tides

Scott L England[1], Robert R. Meier[2], Harald U. Frey[3], Stephen B Mende[3], Andrew W. Stephan[4], Christopher Scott Krier[1], Chihoko Y. Cullens[3], Yen-Jung Joanne Wu[3], Colin C Triplett[5], Martin M Sirk[5], Eric Korpela[3], Brian J Harding[6], Christoph R Englert[7], and Thomas J. Immel[3]

[1]Virginia Polytechnic Institute and State University
[2]George Mason University
[3]University of California, Berkeley
[4]U.S. Naval Research Laboratory
[5]University of California Berkeley
[6]UC Berkeley
[7]Naval Research Laboratory

November 28, 2022

Abstract

In near-Earth space, variations in thermospheric composition have important implications for thermosphere-ionosphere coupling. The ratio of O to N_2 is often measured using far-UV airglow observations. Taking such airglow observations from space, looking below the Earth's limb allows for the total column of O and N_2 in the ionosphere to be determined. While these observations have enabled many previous studies, determining the impact of non-migrating tides on thermospheric composition has proved difficult, owing to a small contamination of the signal by recombination of ionospheric O^+. New ICON observations of far UV are presented here, and their general characteristics are shown. Using these, along with other observations and a global circulation model we show that under certain circumstances the impact of non-migrating tides on thermospheric composition can be observed. By comparing the amplitude of the variation seen with that in the model, both the utility of these observations and a pathway to enable future studies is shown.

First results from the retrieved column O/N2 ratio from the Ionospheric Connection Explorer (ICON): Longitudinal structures induced by nonmigrating tides

By Scott L England

WORD COUNT 10791 TIME SUBMITTED 20-MAY-2021 08:08AM
PAPER ID 72363129

First results from the retrieved column O/N_2 ratio from the Ionospheric Connection Explorer (ICON): Longitudinal structures induced by nonmigrating tides

Scott L. England[1], R. R. Meier[2,4], Harald U. Frey[3], Stephen B. Mende[3], Andrew W. Stephan[4], Christopher S. Krier[1], Chihoko Y. Cullens[3], Yen-Jung J. Wu[3], Colin C. Triplett[3], Martin M. Sirk[3], Eric J. Korpela[3], Brian J. Harding[3], Christoph R. Englert[4] and Thomas J. Immel[3]

[1] Aerospace and Ocean Engineering, Virginia Polytechnic Institute and State University, Blacksburg, United States

[2] Department of Physics and Astronomy, George Mason University, Fairfax, United States

[3] Space Sciences Laboratory, University of California Berkeley, Berkeley, United States

[4] U.S. Naval Research Laboratory, Washington DC, United States

Corresponding author: Scott L. England (englands@vt.edu), Orcid: 0000-0001-5336-0040

Key points

1. An initial overview of the ICON FUV sub-limb observations and derived column O/N_2 ratios is presented
2. In the morning, away from the equatorial ionosphere, the impact of non-migrating tides on O/N_2 is shown clearly for the first time

3. Comparison of the tidal signature with the TIEGCM model highlights basic agreement, with possible discrepancy in tidal vertical wavelength

Abstract

In near-Earth space, variations in thermospheric composition have important implications for thermosphere-ionosphere coupling. The ratio of O to N_2 is often measured using far-UV airglow observations. Taking such airglow observations from space, looking below the Earth's limb allows for the total column of O and N_2 in the ionosphere to be determined. While these observations have enabled many previous studies, determining the impact of non-migrating tides on thermospheric composition has proved difficult, owing to a small contamination of the signal by recombination of ionospheric O^+. New ICON observations of far UV are presented here, and their general characteristics are shown. Using these, along with other observations and a global circulation model we show that under certain circumstances the impact of non-migrating tides on thermospheric composition can be observed. By comparing the amplitude of the variation seen with that in the model, both the utility of these observations and a pathway to enable future studies is shown.

Plain Language Summary

At high altitude in the atmosphere, mixing of the gas via turbulence becomes less important, and mix of atmospheric species begins to vary with altitude, depending on the mass of the atom or molecule. At these altitudes, the composition of the atmosphere can vary greatly with location and time in a manner not seen in the lower levels of the atmosphere. This same high-altitude region overlaps with the charged particle environment known as the Earth's ionosphere. How the

atmosphere and ionosphere interact is in-part determined by the composition of the atmosphere. Measuring this composition is therefore important and is done regularly using observations in the far ultraviolet. These reveal much of the compositional variation, but a small contaminating signal from the ionosphere has made detecting some small changes produced by waves in the atmosphere a challenge. Here, new observations in the far UV are introduced and their general properties shown. By selecting a specific location and time and utilizing supporting data and a global model we are able to show the change in the composition produced by a certain class of wave in the atmosphere. This demonstrates the utility of these new observations and provides a pathway to futures studies.

1. Introduction

The ratio of atomic oxygen to molecular nitrogen concentrations in the thermosphere has important consequences for chemical processes in both the atmosphere and the ionosphere. O and N_2 are the dominant species in the middle and upper thermosphere (e.g., Hedin *et al.*, 1977). The density of O affects the production rate of O^+ in the F-region ionosphere (primarily via charge exchange with N_2^+, with a contribution from direct ionization of O; e.g. Torr and Torr, 1985). The lifetime of O^+ at F-region altitudes is governed by dissociative recombination with N_2 (e.g., Schunk, 1983). Thus, measuring the ratio of O to N_2 provides essential knowledge of the ionospheric state. An effective technique for determination of the thermospheric O/N_2 ratio exists in simultaneous observation of photoelectron generated far ultraviolet (FUV) airglow from O (the 135.6 nm doublet) and N_2 (the Lyman-Birge-Hopfield, LBH band). Strickland *et al.*, [1995] demonstrated that earth nadir and sub-limb observations of these airglow emissions can be used to determine the thermospheric column O/N_2 ratio ($\Sigma O/N_2$). Using such sub-limb

observations of the emission rate ratio yields a ratio of O/N_2 column density of these two species from below the observer down to an altitude corresponding to an N_2 column density of 10^{17} cm^{-2}, which is typically an altitude corresponding to 130 – 140 km altitude range in thermospheric models. Such sub-limb FUV observations have been used to provide observations of $\Sigma O/N_2$ from a wide variety of satellite datasets including Polar Bear (Evans *et al.*, 1995), Dynamics Explorer 1 (Nicholas et al., 1997; Strickland et al., 1999), the Thermosphere, Ionosphere, Mesosphere Energetics and Dynamics Global Ultraviolet Imager (TIMED-GUVI; e.g., Zhang *et al.*, 2004) and Global-scale Observations of the Limb and Disk (GOLD; e.g., Oberheide *et al.*, 2020).

One of the many applications of the $\Sigma O/N_2$ measurement is to investigate composition changes associated with atmospheric tides. Non-migrating tides produce clear zonal variations in the thermospheric winds and temperatures at fixed local times, and are a source of significant longitudinal variation in the low-latitude ionosphere (e.g., Sagawa *et al.*, 2005, Immel *et al.*, 2006, Goncharenko *et al.*, 2010). While it is generally considered that modulation of the E-region dynamo by tidal winds is the primary mechanism through which non-migrating tides impact the longitudinal structure of the ionosphere, perturbations to photochemical equilibrium arising from tidal modulation of the $\Sigma O/N_2$ have also been proposed (e.g., England *et al.*, 2010, Zhang *et al.*, 2010).

Atmospheric tides can perturb the ratio of O and N_2 at altitudes above the homopause as a result of the unequal impact of the vertical tidal winds on species with different scale heights. This can be illustrated using the continuity equation for linear, plane-wave perturbations in the absence of rapid diffusion:

$$\frac{\tilde{\rho}_i}{\bar{\rho}_i} \propto \frac{1}{\omega}\left(\frac{\tilde{w}}{H_i} - \nabla \cdot \tilde{V}\right), \quad (1)$$

where $\tilde{\rho}_i/\bar{\rho}_i$ is the density perturbation relative to the mean value for a given species, ω is the wave frequency, $\tilde{w}$ is the vertical velocity perturbation, H_i is the species-dependent scale height and $\tilde{V}$ is the velocity perturbation (e.g., Dudis and Reber, 1976; Cui *et al*., 2014). From Equation 1, it is apparent that the horizontal winds associated with an atmospheric tide modify the density of all species equally, whereas the impact of the vertical wind is inversely proportional to the species scale height. At Mars, where atmospheric tides are particularly large in amplitude, mass spectrometer data have demonstrated a clear inverse scale-height relationship to the tidal perturbations seen in numerous atmospheric species (England *et al*., 2016). At Earth, tidal-induced variations in the density of minor species such as NO have been observed (e.g., Oberheide and Forbes, 2008). The identification of non-migrating tides in FUV sub-limb observations of $\Sigma O/N_2$ has been attempted, where Zhang *et al*., [2010] reported a moderate variation in the $\Sigma O/N_2$ ratio with longitude that appeared to match the patterns expected from the diurnal eastward wavenumber 2 (DE2) and 3 tides (DE3). However, further analysis by Kil and Paxton, [2011] suggested that the origin of this signature was not variation in $\Sigma O/N_2$, but rather a tidal variation in O^+ at high altitude (well above the photoelectron produced O airglow) that was misinterpreted as a variation in O/N_2. This result was further confirmed by Stephan *et al*., [2019] using data in both the FUV and Extreme UV from the LITES instrument on the International Space Station. Such a misinterpretation is possible as O^+ radiative recombination can yield the same 135.6 nm doublet as photoelectron excitation of O, so while the latter is dominant during the daytime, presence of the former can lead to a small degree of error in the determination of daytime $\Sigma O/N_2$. Kil *et al*., [2013] further quantified the impact of O^+ radiative recombination on $\Sigma O/N_2$ determined from TIMED-GUVI observations and showed this was of 5 – 10 % for data

around 15:00 local time (LT) during August – September 2002, at low geomagnetic activity. This is clearly important in the case of identifying the impact of non-migrating tides on $\Sigma O/N_2$, as these produce only a small variation in the composition (~5 % of the zonal mean).

This study has three purposes. The first is to present new $\Sigma O/N_2$ observations from ICON FUV. The general characteristics of these, their variation with solar zenith angle, latitude and season is presented in Section 3. The second is to use these data, along with other observation from ICON and the TIEGCM model to demonstrate that in limited circumstances the impact of non-migrating tides on $\Sigma O/N_2$ can be found using sub-limb FUV observations (Section 4). The third is to determine both the magnitude of the O/N_2 variations produced by non-migrating tides and to identify times when the retrieved $\Sigma O/N_2$ may be impacted by O^+ radiative recombination to a degree that renders this technique unreliable to identify any tidal signatures in $\Sigma O/N_2$ (Section 4).

2. Data

This section describes the ICON observational data used in this study, including $\Sigma O/N_2$, O^+ profiles and NmF2, horizontal winds, neutral temperatures, and 557.7 nm airglow volume emission rate. A description of the TIEGCM model, which uses tides derived from the ICON observations as part of its lower boundary condition is also given.

2.1 Far UV Brightness and $\Sigma O/N_2$

The ICON Far Ultra-Violet Imager (ICON-FUV; Mende *et al.*, 2017) is a spectrographic imager that observes airglow emissions from the Earth's limb and sub-limb simultaneously. Observations are made in two spectral passbands: Short wave (SW) centered on the 135.6 nm OI

doublet, and long wave (LW) capturing a portion of the Lyman-Birge-Hopfield (LBH) N_2 bands centered on 157 nm. The thermospheric $\Sigma O/N_2$ is found by using the brightness observed in these two passbands for the data taken during the daytime below the limb of the Earth, such that the entire vertical column of O and N_2 is captured (Meier, 2021; Stephan *et al.*, 2018). For ICON-FUV, the observed sub-limb airglow comes from approximately 7.5° great circle away from the spacecraft, and represents a slant integral, rather than purely vertical. Thus, these data represent an average over some small horizontal range. Here we use version 04 of the derived $\Sigma O/N_2$ product (open access described in the acknowledgements section). Section 3 presents an analysis of 6 months of these observations, describing their general properties. Section 4 uses these data to investigate atmospheric tides and highlight their utility and current limitations.

2.2 Extreme UV observations and O^+ altitude profiles

The ICON Extreme Ultraviolet Spectrograph (ICON-EUV; Sirk *et al.*, 2017) is an imaging spectrometer that observes airglow emissions from the Earth's limb in a spectral range from 54 – 88 nm. The altitude profile of O^+ is estimated using daytime observations of the 61.7 nm O^+ triplet and the 83.4 nm O^+ triplet (Stephan *et al.*, 2017). Here we use version 03 of the derived O^+ density profiles and corresponding ionospheric NmF2 values. These data are used in Section 4 to identify the signature of atmospheric tides in the ionospheric O^+.

2.3 Horizontal vector winds and 557.7 nm airglow

The ICON Michelson Interferometer for Global High-Resolution Thermospheric Imaging (ICON-MIGHTI; Englert *et al.*, 2017) is a Doppler Asymmetric Spatial Heterodyne (DASH) spectrometer that observe airglow emissions from the Earth's limb in the visible and near

infrared range. Observations of the visible emission from atomic oxygen at 630.0 nm and 557.7 nm are used to determine line-of-sight Doppler shifts. By employing two orthogonal line of sight measurements of the limb, the horizontal wind velocity is retrieved at altitudes between 90 and 300 km (Harding *et al.*, 2017). Here we use version 04 of the derived horizontal vector winds and relative volume emission rate of the 557.7 nm emission. These data are used in Section 4 to both identify the atmospheric tides present in the lower and middle thermosphere and provide a lower boundary condition to the TIEGCM model.

2.4 O_2 Atmospheric band temperatures

ICON-MIGHTI observations of the near infrared O_2 Atmospheric band around 762 nm are used to determine the lower thermospheric temperature (Stevens *et al.*, 2018). Here we use version 04 of the derived atmospheric temperatures. These data are used in Section 4 to both identify the atmospheric tides present in the lower thermosphere and provide a lower boundary condition to the TIEGCM model.

2.5 TIEGCM simulated ΣO/N2

For comparison with and interpretation of ICON measurements in Section 4, ΣO/N2 are also computed from the Thermosphere-Ionosphere-Electrodynamics General Circulation Model for the Ionospheric Connection Explorer (TIEGCM-ICON; Maute, 2017). This version of the TIEGCM V2.0 model (see http://www.hao.ucar.edu/modeling/tgcm/tiegcm2.0) uses atmospheric tides derived from the ICON-MIGHTI wind and temperature data to perturb its lower boundary (at ~97 km altitude) for simulation of the thermospheric and ionospheric conditions that best correspond to those present during the ICON mission. The tidal lower boundary uses the Hough

Mode Extension (HME) technique and the ICON data to provide a global specification of the tidal spectrum (Forbes *et al*., 2017, Cullens *et al*., 2020). Here we use version 01 of the HME lower boundary forcing from ICON. The neutral wind and $\Sigma O/N_2$ computed with TIEGCM are available at doi:10.7294/14495640.

3. An examination of the retrieved ΣO/N2

This section will present the observed properties of the FUV brightness and retrieved $\Sigma O/N_2$ ratios. Using the first 6 months of 2020 as an example, the key properties will be highlighted, along with some seasonal trends.

3.1 Observed FUV brightness

Insight into the ICON FUV dataset can be gained by examining the brightness observed in the SW and LW channels over a range of conditions. Figure 1 shows the observed brightness in both channels for one day of observations (March 15th, 2020 is shown here as an example from approximately the middle of the 6-month dataset that will be examined here). The location of the observations for this day are shown in terms of latitude, LT and solar zenith angle (SZA) of the intersection of the instrument's line of sight with a surface at 150 km altitude above the geoid (corresponding to the location of the $\Sigma O/N_2$ measurement). For this day, the daytime data are all located within the northern hemisphere, but this varies with orbital precession. Each of the observations shown represents a measurement from a 12 second exposure. As expected, both the SW and LW channels show a strong variation in brightness with SZA as this is the primary factor in determining the total rate of photoelectron production, which is the dominant excitation process for the emission seen at these wavelengths. This correlation is clear in Figure 1, as is the

related local time influence on the brightness observed. Very little scatter beyond these geometric trends is seen. The relative brightness between the two channels is reflective of the passbands and the relative brightness of the oxygen and nitrogen-related dayglow (see Mende *et al.*, 2017).

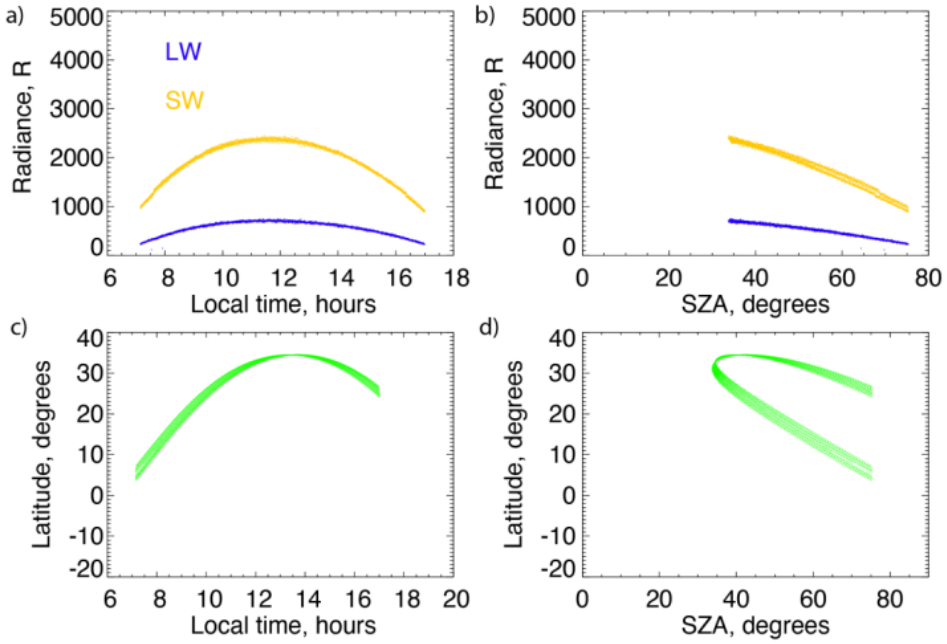

Figure 1 Observed sub-limb FUV SW and LW airglow brightness for March 15, 2020. Panel a shows the brightness of the two airglow features as a function of local time. Panel b shows the brightness of the two airglow features as a function of solar zenith angle. In Panels a and b, the yellow points correspond to the SW airglow passband and the blue points correspond to the LW airglow passband. Panel c shows the location of the observed points, as a function of latitude and local time. Panel d shows the location of the observed points, as a function of latitude and solar zenith angle.

Figure 2 shows the observed brightness over a 45-day period, which allows ICON to sample a full range of latitudes and local times due to orbital precession. Here the first 45 days of 2020 are shown, corresponding to nearby solstice conditions with an associated strong latitudinal asymmetry in SZA (not shown). SZA dependence of the brightness of both the SW and LW channel data is evident, with the brightest emissions seen near the subsolar point (close to noon in the southern hemisphere) and the dimmest emissions seen near the terminators.

Taking the ratio of the SW to LW brightness (Figure 2c) eliminates some of the strong SZA dependence and allows for a first-order view of the impacts of varying $\Sigma O/N_2$ on the emissions. Plotting this ratio for all the points in the 45-day period reveals two overlapping patterns. First is the strong gradient in latitude, with the highest SW/LW ratios tending to be seen at higher northern latitudes. The second is a change with season as the later days within this range show generally higher SW/LW ratios at all latitudes (seen in the orange colors appearing diagonally from the northern higher latitudes at early LT to southern latitudes at later LT). Both of these patterns can be understood in terms of the expected seasonal variation in $\Sigma O/N_2$, with lower $\Sigma O/N_2$ expected in the summer hemisphere near solstice and generally higher $\Sigma O/N_2$ expected across this region nearer equinox (see Jones Jr *et al.*, 2018 and references therein). The variation in the $\Sigma O/N_2$, derived using these data, is examined in the following section.

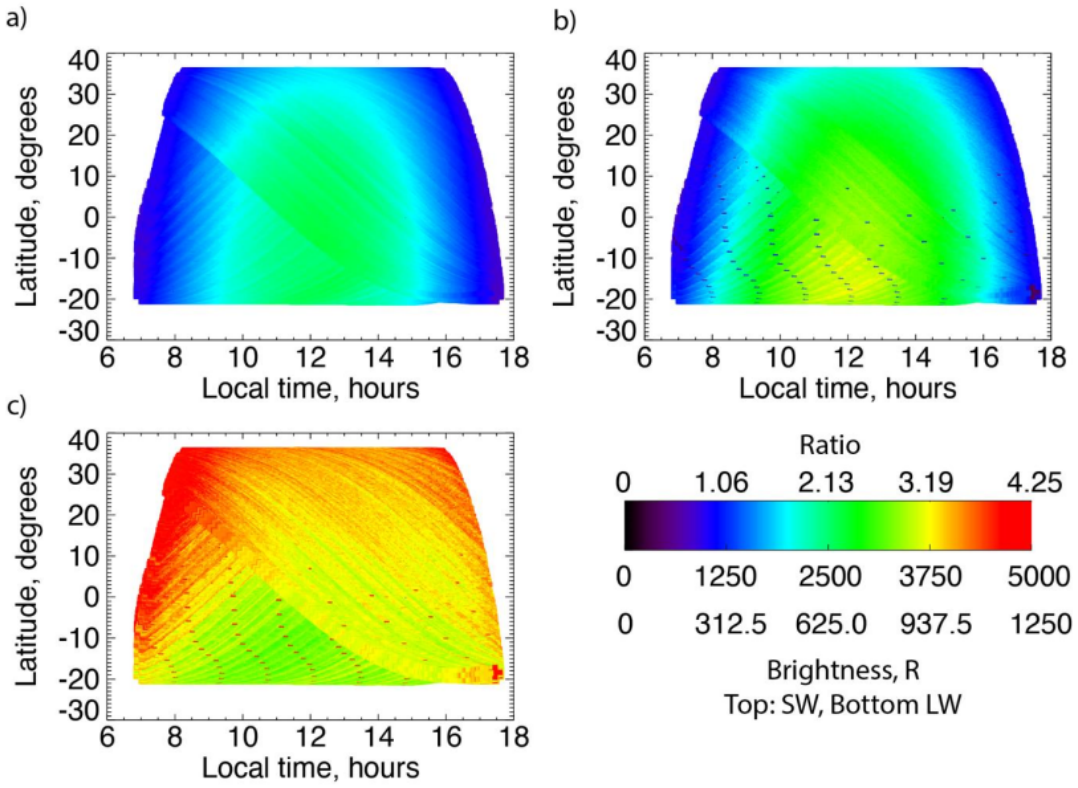

Figure 2 Brightness of the SW and LW airglow and their ratio for days 1 – 45 of 2020. Panel a shows the brightness of the SW airglow as a function of latitude and local time. Panel b shows the brightness of the LW airglow as a function of latitude and local time. Panel c shows the ratio of the brightness of the SW to the brightness of the LW airglow as a function of latitude and local time.

3.2 Observed ΣO/N_2

Figure 3 shows the retrieved ΣO/N_2 for January 2nd, 2020. For this example, the observations cover two portions of the latitude – SZA parameter space such that one covers all dayside SZA at a near constant latitude in the southern hemisphere and the other spans latitude with increasing SZA. This yields two examples of the variations expected in ΣO/N_2, if these were the dominant

controlling factors. This is revealed by a comparison to NRLMSISE-00 (Picone *et al.*, 2002; MSIS hereafter). While a newer version of the MSIS model exists (Emmert *et al.*, 2020), the earlier version is used here to allow for a comparison to published results from TIMED-GUVI, described below. The predicted $\Sigma O/N_2$ from MSIS show two clear patterns with SZA, corresponding to the two regions of observation. The ICON values reveal some evidence of this bifurcated pattern but with a much smaller difference between the two regions and also clear geophysical variability about this trend. Further, the $\Sigma O/N_2$ values retrieved from ICON observations are lower than MSIS for almost all cases. These two observations are worth considering in more detail. First, the variation in the retrieved values is compared to the uncertainty determined for each value, shown in panel c of Figure 3. The uncertainties clearly increase slightly with increasing SZA. This may be expected as the photoelectron production peak rises in altitude with increasing SZA and thus the $\Sigma O/N_2$ is less sensitive to N_2 at lower altitudes, thereby increasing the uncertainty in the $\Sigma O/N_2$. At lower SZA, the uncertainties are well within ~5 – 10% of the retrieved value, and smaller than the spread seen in Figure 3b, suggesting that significant geophysical variability is present on this day. Second, the systematic difference with MSIS is examined using a larger data sample, to avoid any issues with conditions on a single day. Using 180 days, the ratio of the retrieved $\Sigma O/N_2$ from ICON is compared to that predicted with MSIS, and shown vs LT in Figure 3d. While significant spread in these values is seen, the mean at each LT is relatively constant and below 1 for each one-hour LT bin. Further, it is worth noting that a large portion of the spread that is visible comes from the points below the 5th and above the 95th percentile (see orange lines in Figure 3d). Taking an average over all LT, the mean value of the ICON/MSIS ratio is 0.84, with a standard deviation of 0.089 (approximately 10%). Meier *et al.* [2015] reported a similar offset when comparing TIMED-

GUVI $\Sigma O/N_2$ values to MSIS. Considering only the values from 2007 (near solar minimum), Meier *et al*. [2015] reported a ratio of 0.89 (see their Figure 20). Given that the ICON and GUVI datasets do not span the same time or latitude range, the overall agreement in these values is within the uncertainties of the two datasets and suggests that the ICON $\Sigma O/N_2$ values (which come from sub-limb observations) are in family with those reported by Meier *et al*., [2015] using the GUVI limb observations.

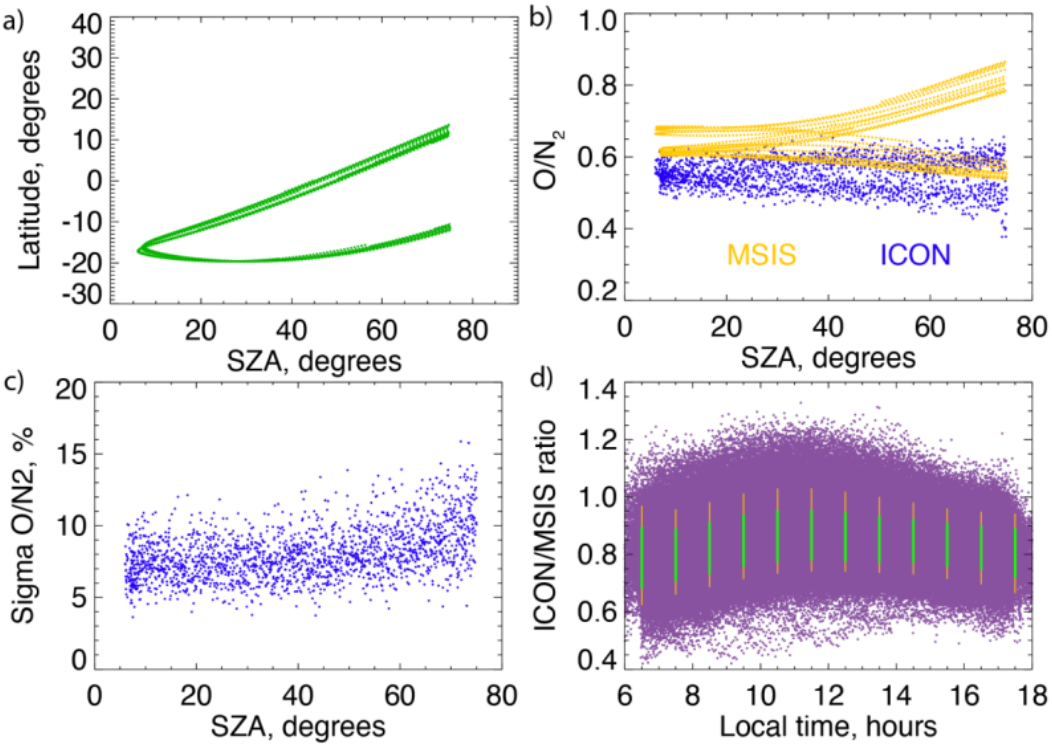

Figure 3 Retrieved $\Sigma O/N_2$ compared to the MSIS model. Panel a shows the location of the observations on January 2, 2020 as a function of latitude and solar zenith angle. Panel b shows the retrieved $\Sigma O/N_2$ from ICON and the MSIS model for each point observed during January 2, 2020, as a function of solar zenith angle. Panel c shows the one standard deviation uncertainty in each of the retrieved $\Sigma O/N_2$ from ICON for each point observed during January 2, 2020, as a

function of solar zenith angle. Panel d shows the ratio between the retrieved ΣO/N$_2$ from ICON and the MSIS model for each observation made during the first 6 months of 2020, as a function of local time. The purple dots represent the value for each observation. The green lines show the mean and standard deviation of these points at each 1-hour interval, and the orange line show the range from the 5th to the 95th percentile points at each 1-hour interval. The average ratio between ICON and MSIS is 0.84 and the average of the standard deviations is 0.089.

Figure 4 shows the effect of seasonal changes on the ΣO/N$_2$ retrieved from ICON and predicted from MSIS. Here only values near to local noon (11 – 13 hours LT) are shown as this both eliminates any LT variation that may confuse the seasonal changes and limits the data to the region with the lowest measurement uncertainty. Each panel represents the data from a 45-day period, in which panels a and b correspond to days 1 – 45 (post northern winter solstice; matching Figure 2), panels c and d correspond to days 46 – 90 (approaching equinox) and panels e and f correspond to days 136 – 180 (approaching northern summer solstice). For days 1 – 45, a strong gradient with latitude is seen, as expected from Figure 2 and consistent with the seasonal variations reported in O/N$_2$ (e.g., Jones Jr *et al.*, 2018). Following this semi-annual and annual pattern, the values close to solstice are generally higher at all latitudes and the latitudinal gradient is essentially reversed by days 136 – 180. All seasonal changes are seen in the MSIS values, indicating that the seasonal trends in ICON retrieved ΣO/N$_2$ values vary are in agreement with previous observations.

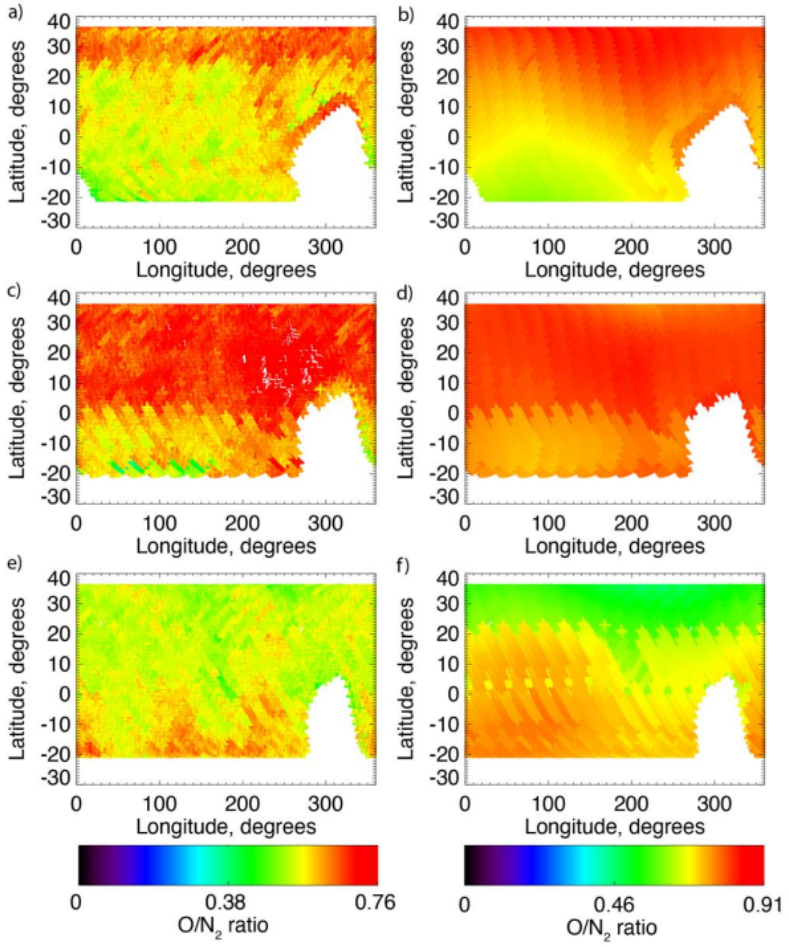

Figure 4 geographic variation in the ΣO/N_2 from ICON and MSIS. Panels a, c and e show the ICON values and panels b, d, and f show the MSIS values. Panels a and b are for days 1 – 45, 2020. Panels c and d are for days 46 – 90, 2020. Panels e and f are for days 136 – 180, 2020. All values are from 11 – 13 hours local time. Note the different color scales used for the ICON and MSIS values, such that the variations with latitude and season are visible. Note that data are available in the southern hemisphere near 300 degrees longitude as these remote observation locations correspond to when the ICON spacecraft is within the South Atlantic Anomaly.

4. The signature of nonmigrating atmospheric tides in the $\Sigma O/N_2$

Using the $\Sigma O/N_2$ values retrieved from ICON, we can examine the signature of non-migrating tides on the composition of the middle thermosphere. The first step is to select a time period when non-migrating tides are seen clearly, such that their signature can be identified. This is accomplished with a tidal analysis of the MIGHTI horizontal wind and temperature data (e.g., Cullens *et al.*, 2020). Figure 5 shows the amplitude of the diurnal eastward wavenumber 3 (DE3) and semi-diurnal eastward wavenumber 2 (SE2) tides as functions of latitude and day of year for the first 100 days of 2020 at 97 km altitude (where temperature and horizontal wind data are available through at all local times). The DE3 is known to have a peak in amplitude around February – March during most years (e.g., Oberheide and Forbes, 2008). Indeed, a peak is seen in Figure 5e around days 30 – 90 in the meridional winds near the equator and in Figure 5c, around days 60 – 100 in the zonal winds north of the equator. SE2 is the second strongest non-migrating tide during this time period that also produces a wavenumber-4 signature in a fixed LT frame (the diurnal westward 5, semi-diurnal westward 6, terdiurnal eastward 1 tides can also produce wavenumber-4 signatures but were found to be of negligible amplitude during this time period). This is seen to be weaker than DE3 throughout this time period, but is still present with some measurable amplitude, especially in the meridional winds around days 60 – 100.

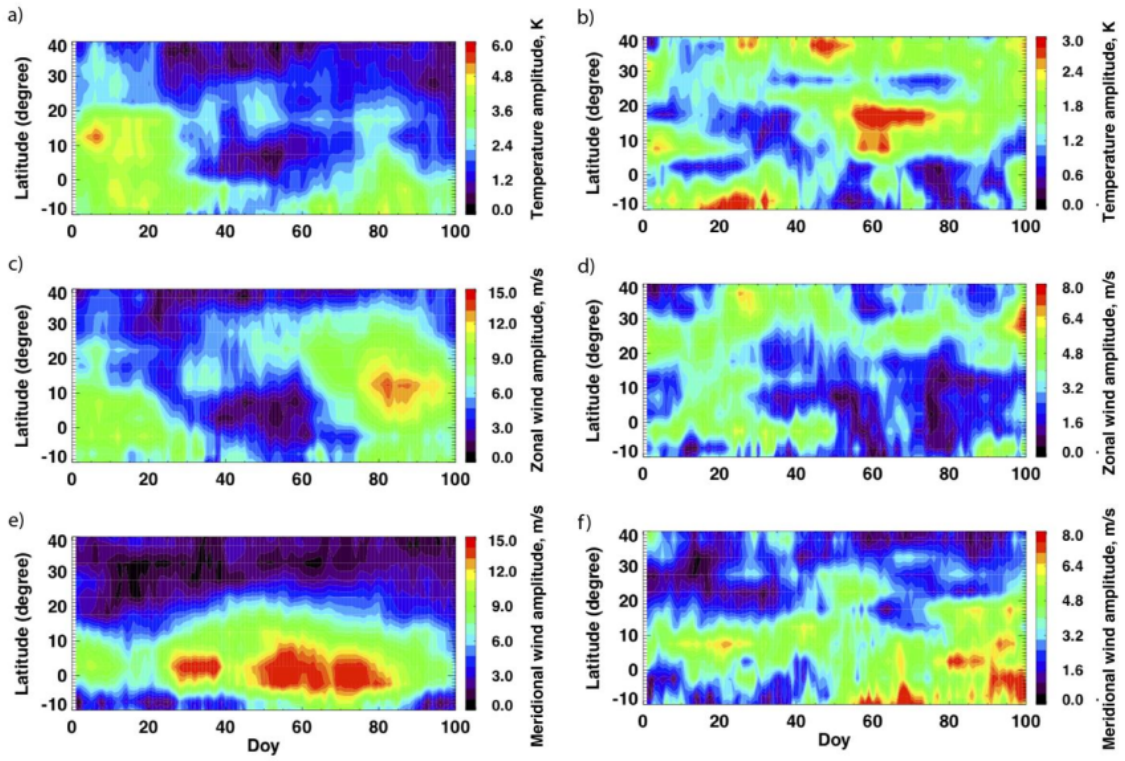

Figure 5 Amplitude of the DE3 and SE2 non-migrating tides observed by MIGHTI at 97 km altitude during the first 100 days of 2020. Panels a, c and e correspond to the DE3 tide and panels b, d and f correspond to the SE2 tide. Panels a and b show the temperature amplitude, panels c and d show the zonal wind amplitude and panels e and f correspond to the meridional wind amplitude. All values are shown at 97 km altitude, corresponding to the lower boundary of the TIEGCM model. Note the different scales used in each panel.

Figure 5 shows the tides determined at the base of the thermosphere, where the temperature and wind fields are available at all LT (which are required to provide the lower boundary forcing for the TIEGCM model). With the knowledge that the dominant non-migrating tides are associated with eastward moving wavenumber-4 signatures in a fixed LT frame, we can examine

corresponding wavenumber-4 signatures in the winds near the photoelectron production peak. In the case of ICON-MIGHTI observations, daytime observations are consistently available near 150 km using the 557.7 nm observations. Using daytime only observations, it is not possible to identify the full tidal spectrum, but the variation in phase of any tidal signature with LT can help to identify which tides may be present at this altitude. Figure 6 shows the wavenumber-4 component of the averaged meridional and zonal winds between 150 km and 160 km altitude, averaged over days 75 – 100 (when DE3 is seen to be strongest). This figure uses data from 25 – 35° north, to correspond to the $\Sigma O/N_2$ values examined below. A clear eastward moving signature is seen in both the zonal and meridional winds and is clearest in the zonal winds. This may be expected as the symmetric component of DE3 becomes dominant over the antisymmetric component with increasing altitude in the thermosphere, and is primarily characterized by zonal winds, rather than meridional winds (e.g. Oberheide and Forbes, 2008). The best fit phase shift in the zonal wind and meridional wind (shown with the dotted black line) is 5.12° / hour and 7.00° / hour, respectively. The phase shifts of the zonal wind and meridional wind fall between that expected for DE3 (3.75° / hour) and SE2 (7.5° / hour) and is consistent with a mixture of these two waves being present, as indicated from the lower-altitude data (Figure 5).

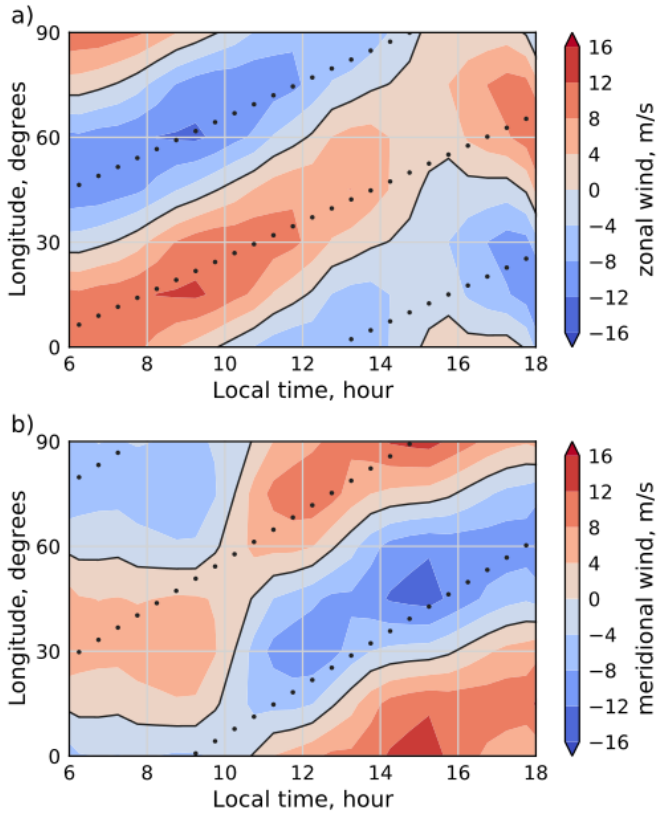

Figure 6 Wavenumber-4 component of the horizontal winds observed by MIGHTI as functions of longitude and local time. Panel a shows the zonal wind perturbation and panel b shows the meridional wind perturbation. All data represent the wavenumber-4 fit to the data that are averaged over days 75 – 100, 2020, altitudes from 150 – 160 km altitude and 25 – 35° north. The best-fit linear trend in the zonal wind (meridional wind) of 5.12° (7.00°)/ hour is shown with the black dotted lines.

The eastward moving non-migrating tides seen in Figure 5 and Figure 6 are expected to produce a wavenumber-4 signature in the $\Sigma O/N_2$ when viewed in a fixed LT frame. Figure 7 shows the

wavenumber-4 component of the $\Sigma O/N_2$ retrieved from ICON as functions of LT and day of year (DOY). Note that the LT sampled at any given latitude decreases with increasing day of year due to orbit precession. Data are shown at 25 – 35° north, where the DE3 is still seen clearly in MIGHTI data and the impact of any O^+ radiative recombination is lower than near to the equator. The wavenumber-4 fit is performed for each day, and these are shown with both the corresponding LT and day of year. As the observations at this latitude range on a single day are sampled at two LT, the data are split into ascending and descending portions of the orbit. The ascending portion samples this latitude range during daytime from DOY 64 – 81, whereas the descending portion covers DOY 75 – 93. Figure 5 suggests that the DE3 tide is strongest between DOY 75 – 93 of this range but is clearly present throughout this entire range. The ascending portion sees a clear wavenumber-4 structure in the $\Sigma O/N_2$ between DOY 75 – 81, corresponding only to LT before 11 hours. With just ~3 hours of LT covered, no clear phase progression is evident. After ~11 LT (before DOY 75), the signal is less clear, which could be evidence of O^+ radiative recombination, a weaker tidal signature at this DOY range, or a change in the tidal signature with LT. Examining the data from the descending portion of the orbit, a clear wavenumber-4 signature is seen moving eastwards with LT between DOY 82 – 93 (corresponding to LT 7.4 – 12.9 hours). With ~5.5 hours of LT, the phase speed can be estimated, and appears to match that of DE3 (shown by the black line). The amplitude seen during this DOY range is ~3 – 4 % of the zonal mean value. As with the data from the ascending portion of the orbit , the data at later LT show a less clear signature. However, for the descending portions these cover DOY 75 – 82, when the ascending portion still sees a strong signature, ruling out a weaker tidal signature at these DOY as the origin of this. This leaves the change in

tidal signature with LT and a contribution of O^+ radiative recombination as possibilities for the change in characteristic of the wavenumber-4 pattern seen at later LT.

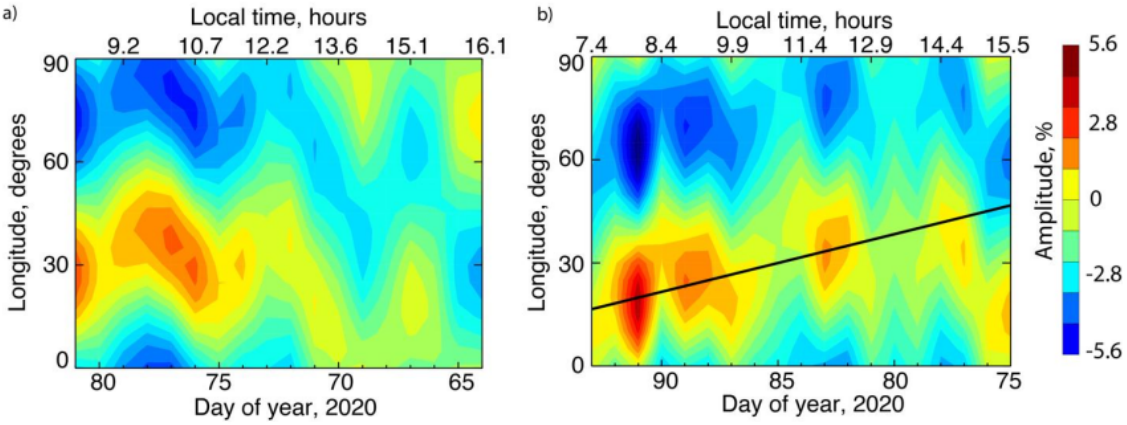

Figure 7 Wavenumber-4 component of the perturbation in the $\Sigma O/N_2$ retrieved from the ICON observations as functions of day of year, local time and longitude. Panel a shows the data from the ascending portion of the orbit and panel b shows the data from the descending portion of the orbit. All data are averaged over 25 – 35° north. The amplitude of the $\Sigma O/N_2$ perturbation is determined relative to the mean value at each day of year (corresponding to a single local time). The solid line shown in panel b indicates the phase shift with local time expected for the DE3 tide and is included as a visual guide.

Using the tides identified in the upper mesosphere and lower thermosphere region (Figure 5 and similar) and the HME fits to these (Forbes *et al.*, 2017) it is possible to perturb the lower boundary of the TIEGCM model (near 97 km altitude) such that it reproduces the tides observed by ICON (Maute *et al.*, 2017). This is instructive as, assuming the TIEGCM model can replicate the propagation of these tides to ~150 km altitude, the model can be used to compute the $\Sigma O/N_2$

perturbation that would be expected given the tides present on these days and to explore differences between the modeled and observed O/N_2. Figure 8 shows the wavenumber-4 pattern in the neutral winds at 150 km altitude and the $\Sigma O/N_2$ from TIEGCM as a function of local time. The model results come from an average over DOY 75 – 95 when ICON sees the strongest $\Sigma O/N_2$ signature. The results are shown at 25 – 35° latitude to match the ICON wind observations in Figure 6 and ICON $\Sigma O/N_2$ in Figure 7. In the TIEGCM results, an eastward motion of the perturbation in all parameters with a phase speed matching that of DE3 is clearly evident across all daytime LT. The amplitude of the horizontal wind perturbations match those observed by ICON well, confirming that the model is reproducing the propagation of a dominant DE3 tide up to 150 km altitude, in overall agreement with these observations. A slight phase shift is seen, which may imply that the vertical wavelength of the tide is different in the model compared to that observed. The vertical winds, which are not observed, also show a similar eastward motion that very closely matches that expected for DE3. The $\Sigma O/N_2$ likewise shows an eastward propagation that is similar to that in the winds. The amplitude of the signature shows some variation with LT, as may be expected given the presence of the SE2 perturbation, such that the amplitude seen before ~9 LT is the largest, although the amplitude is also large between ~12 – 15 LT. The maximum amplitude seen in $\Sigma O/N_2$ at any time is ~2% which is a factor of 1.5 – 2 times smaller than the pre-noon values observed by ICON. As this is primarily produced by the vertical wind perturbation, it can be assumed that the vertical wind perturbation in the TIEGCM model is smaller than that in the atmosphere, although no direct observations exist to confirm this. Such a mismatch in the vertical wind would also be consistent with a mismatch in the vertical wavelength of the tide in the model compared to the atmosphere. The strength of the $\Sigma O/N_2$ signature in the 12 – 15 LT range suggests that ICON may be expected to see a clear

signature at this time. This would indicate that the presence of an O^+ radiative recombination signal is the most likely cause of the changes observed in Figure 7 after ~13 LT.

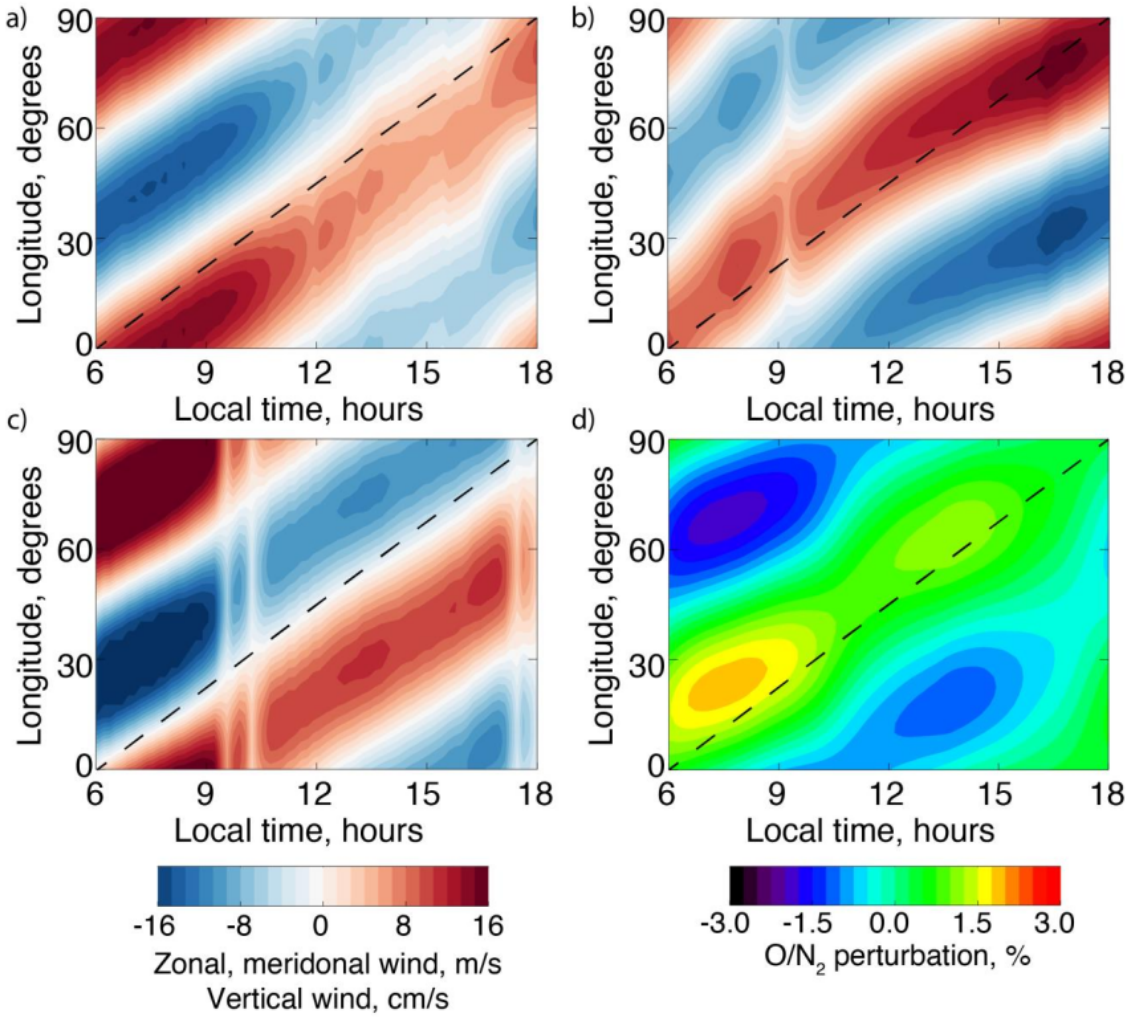

Figure 8 Wavenumber-4 perturbation in the neutral winds and ΣO/N_2 ratios from the TIEGCM model as functions of local time and longitude. Values are averaged over 25 to 35° north and over days 75 – 95 of 2020. Panels a – c show the perturbation in the zonal, meridional and vertical wind respectively. The horizontal winds are shown in m/s and the vertical wind is shown in cm/s. Panel d shows the perturbation to the ΣO/N_2 and is expressed as a percentage of the

zonal mean value at each local time. The dashed black line shows a phase shift of 3.75° / hour as would be expected from a DE3 tide.

To investigate the possibility of O^+ radiative recombination contaminating the wavenumber-4 $\Sigma O/N_2$ perturbations seen with ICON, we make use of the ICON EUV O^+ observations. Any potential O^+ radiative recombination can be estimated from examining both the column O^+ and NmF2 values determined from these data. Figure 9 shows the wavenumber-4 perturbation in NmF2 and O^+ as functions of longitude and local time. Here only the descending portion data are shown, which provides observations at an overlapping DOY range as the clearest signal in the $\Sigma O/N_2$ observations. In both parameters from the EUV instrument, a significant wavenumber-4 signature is seen after ~13 LT, and only a much weaker signature is seen prior to this time. From ~13 – 16.9 LT there is some evidence of an eastward motion in these perturbations, but over such a short range of LT the rate of these is difficult to determine. Nonetheless, these data suggest that the wavenumber-4 O^+ radiative recombination signal would move eastwards with increasing local time and have become increasingly significant after ~13 LT. If the O^+ radiative recombination signal is not in phase with the $\Sigma O/N_2$ signature, this could therefore account for the inconsistent wavenumber-4 signature seen in Figure 7 after ~12 LT.

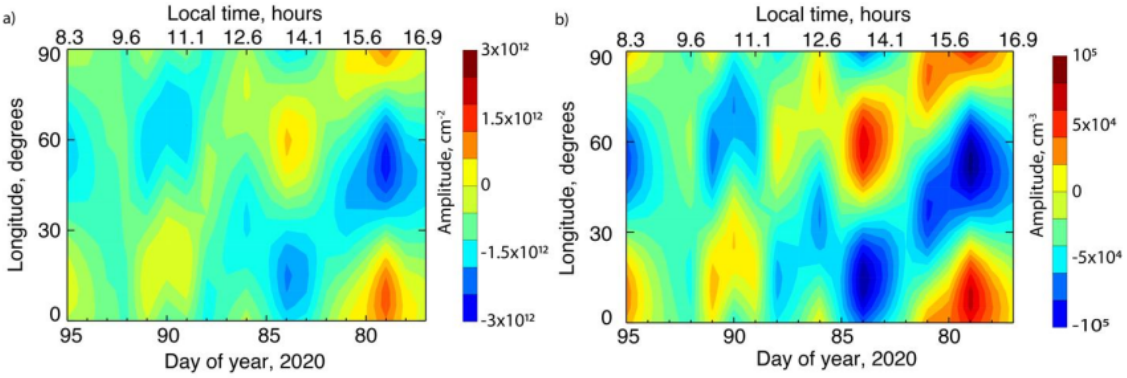

Figure 9 Wavenumber-4 component of the pertrubation in ionospheric nmF2 and column O^+ abundance retrieved from ICON EUV observations as functions of day of year and longitude. Panel a shows the perturbation in the total column O^+ and panel b shows the perturbation in the NmF2 value. All data are from the descending portion of the orbit and are averaged over 25 – 35° north.

Shepherd *et al.*, (2011) reported a wavenumber-4 variation in the brightness of the O(^{1}S) 557.7 nm airglow near 250 km altitude. The ICON MIGHTI instrument is able to measure the brightness of this emission at 150 km altitude, close to the photoelectron peak and the neutral winds as shown in Figure 6. At this altitude, the brightness of this emission is believed to be produced mainly by $N_2(A^3\Sigma_u^+)$ + O, where the excited N_2 is the minor species and is produced by photoelectron impact on N_2 (see Zhang and Shepherd, 2005 and references therein). This means that its variation in brightness may be expected to be in antiphase with the O/N_2 variations seen in Figure 7 and Figure 8. Figure 10 shows the observed wavenumber-4 perturbation in the 557.7 nm airglow observed with the 'forward' looking MIGHTI field of view (MIGHTI-A). Data are taken over DOY 75 – 100 to provide both overlap when the clear signature is seen in Figure 7 and provide sufficient LT coverage at the latitude range of these ΣO/N_2 observations. Once

again, a clear eastward moving signature is seen throughout all daytime hours. As in Figure 6 and Figure 8, a variation in the amplitude of the signature is seen with LT and the eastward motion does not perfectly match that of DE3, suggesting that SE2 is present as well with some magnitude. The perturbation is also seen to be in near antiphase with the $\Sigma O/N_2$ observations in Figure 7 and model results in Figure 8. This provides confidence that the N_2 densities in the model are varying in a manner consistent with the atmosphere at this time, and implies that the O densities should do likewise, as both respond to the same vertical wind perturbations.

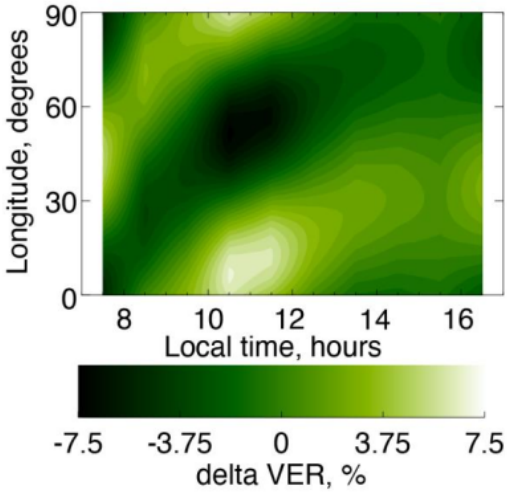

Figure 10 Wavenumber-4 perturbation of the 557.7 nm airglow observed by MIGHTI Channel A as a function of local time and longitude. All data are averaged over days 75 – 100, 2020, tangent altitudes from 150 – 160 km altitude and 25 – 35° north. All values are expressed as a percent of the zonal mean value.

5. Conclusions

A survey of six months of ICON FUV sub-limb observations and retrieved $\Sigma O/N_2$ from 2020 is presented. From these we see variations in both the brightness of the airglow and $\Sigma O/N_2$ that

exhibit the expected SZA, latitudinal and seasonal variations. The uncertainties in the retrieved $\Sigma O/N_2$ increase slightly with SZA as may be expected given the variation in the photoelectron production altitudes with SZA. Uncertainties on single 12 second data points generally fall in the 5 – 10 % range except at large SZA. A comparison of the retrieved $\Sigma O/N_2$ and those predicted using NRL-MSISE00 show a consistent bias such that the ICON values are around 0.84 times the MSIS values, which is in good agreement with an analysis of TIMED-GUVI observations at solar minimum reported by Meier *et al*., [2015].

An examination of the impact of non-migrating tides on the $\Sigma O/N_2$ is presented. This is done by focusing on a time period in early 2020 when ICON clearly sees the DE3 non-migrating tide in the winds and temperatures near the base of the thermosphere, and the winds at 150 km altitude. At this time, some SE2 is also observed, contributing to the wavenumber-4 signature in fixed local time in addition to DE3. Following prior studies, we examine the observations away from the equator in an attempt to minimize the effect of O^+ radiative recombination and focus on a region from 25 – 35° north where we have data from all instruments on nearly the same DOY. Using the tides observed in the MLT region as a lower boundary condition, we also perform a simulation with the TIEGCM model to provide context for the ICON observations. From these we see a wavenumber-4 perturbation in the retrieved $\Sigma O/N_2$ that is small (below ~5% of the zonal mean value). During the morning, the signal is comparatively clear and can be seen to move eastwards with increasing local time, but this pattern breaks down in the afternoon. Three reasons for this morning to afternoon change are considered: a change in the strength of the signature with local time; a change in the strength of the signature with DOY; and the effect of an overlapping wavenumber-4 signature in the O^+ radiative recombination that becomes stronger

517 in the afternoon. From an examination of the ICON observations of $\Sigma O/N_2$ and other parameters,
518 the first two of these are considered to be less likely than the impact of contamination of the SW
519 dayglow signal by radiative recombination, in agreement with Kil and Paxton, [2011] and Kil *et*
520 *al*., [2013]. Other ICON observations clearly shown the presence of a wavenumber-4 pattern
521 generated from DE3 and SE2 is present at the altitude of the photoelectron emissions, the source
522 of the $\Sigma O/N_2$ observations. While these vary with LT, they are clear throughout the daytime.
523 This behavior is also supported by the TIEGCM model, which also shows a clear $\Sigma O/N_2$
524 perturbation should be clear throughout the day. The O^+ data also exhibits wavenumber-4
525 structure in this is present during the afternoon hours that moves east with LT, but is not in phase
526 with the $\Sigma O/N_2$ signature. The O^+ radiative recombination contamination of the SW dayglow
527 signature thus results in the unclear pattern in the retrieved $\Sigma O/N_2$. Using data near 15:00 LT, Kil
528 *et al*., [2013] estimated that the $\Sigma O/N_2$ retrieved was perturbed by ~5 – 10 % by O^+ radiative
529 recombination. This value is larger than tidal impact on $\Sigma O/N_2$ seen here, and is consistent with
530 our finding of the contamination of the dayglow signature during the afternoon. These
531 conclusions underline the limitation of using the retrieved $\Sigma O/N_2$ values retrieved from sub-limb
532 FUV airglow to determine small wave-induced perturbations. But the analysis does demonstrate
533 that the observations can provide a good estimate of the amplitude of the $\Sigma O/N_2$ signature in the
534 morning thermosphere, at least at latitudes away from the peak of the equatorial ionospheric arcs.
535
536 The observed variation in $\Sigma O/N_2$ is generally larger than that in the TIEGCM model at the same
537 time, which suggests the model is underestimating the wavenumber-4 component of the vertical
538 wind that creates the $\Sigma O/N_2$ perturbation. While the TIEGCM model replicates the observed
539 horizontal wind amplitudes near 150 km well, the phase of the wavenumber-4 signature does not

agree with that observed. If the model produces a DE3 tide with the incorrect vertical wavelength, that would also be consistent with both the incorrect horizontal wind phase and vertical wind. This analysis demonstrates the utility of the combined ICON datasets, especially when used in conjunction with first-principles models.

Acknowledgements

This analysis used version 04 of the Level 2.4 ICON-FUV data, version 04 of the Level 2.2 ICON-MIGHTI data, version 02 of the Level 2.6 ICON-EUV data and version 01 of the Level 4.1 HME data which are available from the ICON website (https://icon.ssl.berkeley.edu/Data) and NASA's Space Physics Data Facility (https://cdaweb.gsfc.nasa.gov/pub/data/icon/). The TIEGCM winds and $\Sigma O/N_2$ are available for peer-review purposes at https://figshare.com/s/cc0f288dfd8db77263a3 (following AGU's FAIR data policy, this will be moved to the VT library permanent repository and assigned a DOI once no more changes are to be made). ICON is supported by NASA's Explorers Program through contracts NNG12FA45C and NNG12FA42I. The NRLMSISE-00 model is available from NASA's Community Coordinated Modeling Center (https://ccmc.gsfc.nasa.gov/pub/modelweb/). RRM acknowledges support from ICON via NASA's Explorers Program and the US Civil Service Retirement System.

References

Cui, J., R. V. Yelle, T. Li, D. S. Snowden, and I. C. F. Müller-Wodarg (2014), Density waves in Titan's upper atmosphere, *J. Geophys. Res. Space Physics*, *119*, 490–518, doi:10.1002/2013JA019113.

563

564 Cullens, C.Y., Immel, T.J., Triplett, C.C. *et al*. Sensitivity study for ICON tidal analysis. *Prog*
565 *Earth Planet Sci* 7, 18 (2020). https://doi.org/10.1186/s40645-020-00330-6

566

567 Dudis, J. J., and C. A. Reber (1976), Compositional effects in thermospheric gravity waves,
568 *Geophys. Res. Lett.*, *3*, 727–730, doi:10.1029/GL003i012p00727.

569

570 Emmert, J. T., Drob, D. P., Picone, J. M., Siskind, D. E., Jones, M., Mlynczak, M. G., et al.
571 (2020). NRLMSIS 2.0: A whole-atmosphere empirical model of temperature and neutral species
572 densities. *Journal Geophysical Research*, e2020EA001321. https://doi.
573 org/10.1029/2020EA001321

574

575 England, S. L., et al. (2016), Simultaneous observations of atmospheric tides from combined in
576 situ and remote observations at Mars from the MAVEN spacecraft, J. Geophys. Res. Planets,
577 121, doi:10.1002/2016JE004997.

578

579 England, S.L., T.J. Immel, J.D. Huba, M.E. Hagan, A. Maute, R. DeMajistre, Modeling of
580 multiple effects of atmospheric tides on the ionosphere: an examination of possible coupling
581 mechanisms responsible for the longitudinal structure of the equatorial ionosphere. J. Geophys.
582 Res. 115, 05308 (2010). doi:10.1029/2009JA014894

583

584 Englert, C.R., Harlander, J.M., Brown, C.M., Marr, K.D., Miller, I.J., Stump, J.E., Hancock, J.,
585 Peterson, J.Q., Kumler, J., Morrow, W.H., Mooney, T.A., Ellis, S., Mende, S.B., Harris, S.E.,

586 Stevens, M.H., Makela, J.J., Harding, B.J., and Immel, T.J., 2017. Michelson Interferometer for
587 Global High-resolution Thermospheric Imaging (MIGHTI): instrument design and calibration.
588 Space Science Reviews, 212(1-2), pp.553-584. DOI: 10.1007/s11214-017-0358-4
589
590 Evans, J. S., D. J. Strickland, R. E. Huffman and R. W. Eastes (1995), Satellite remote sensing of
591 thermospheric O/N2 and solar EUV, 2. Data Analysis, J. Geophys. Res., 100, 12,217-12,226.
592
593 Forbes, J. M., Zhang, X., Hagan, M. E., England, S. L., Liu, G., Gasperini, F., (2017). On the
594 specification of upward-propagating tides for ICON science investigations. Space Science
595 Reviews 212: 697. https://doi.org/150.1007/s11214-017-0401-5
596
597 Goncharenko, L.P., J.L. Chau, H.-L. Liu, A.J. Coster, Unexpected connections between the
598 stratosphere and ionosphere. Geophys. Res. Lett. **37**, 10101 (2010). doi:10.1029/2010GL043125
599
600 Harding, B. J., Makela, J. J., Englert, C. R., Marr, K. D., Harlander, J. M., England, S. L., and
601 Immel, T. J., (2017). The MIGHTI wind retrieval algorithm: description and verification. Space
602 Science Reviews, 212: 585. https://doi.org/10.1007/s11214-017-0359-3
603
604 Hedin, A. E., Reber, C. A., Newton, G. P., Spencer, N. W., Brinton, H. C., Mayr, H. G., &
605 Potter, W. E. (1977). A global thermospheric model based on mass spectrometer and incoherent
606 scatter data MSIS, 2. Composition. *Journal of Geophysical Research*, **82**(16), 2148–2156.
607 https://doi.org/10.1029/JA082i016p02148
608

609 Immel, T.J., E. Sagawa, S.L. England, S.B. Henderson, M.E. Hagan, S.B. Mende, H.U. Frey,
610 C.M. Swenson, L.J. Paxton, The control of equatorial ionospheric morphology by atmospheric
611 tides. Geophys. Res. Lett. **33**, 15108 (2006). doi:10.1029/2006GL026161
612
613 Immel, T.J., England, S.L., Mende, S. B. et al., (2018). The Ionospheric Connection Explorer
614 Mission: Mission Goals and Design, Space Science Reviews, 214: 13.
615 https://doi.org/10.1007/s11214-017-0449-2
616
617 Jones Jr., M., Emmert, J. T., Drob, D. P., Picone, J. M., & Meier, R. R. (2018). Origins of the
618 thermosphere-ionosphere semiannual oscillation: Reformulating the "thermospheric spoon"
619 mechanism. *Journal of Geophysical Research: Space Physics*, *123*, 931–954.
620 https://doi.org/10.1002/2017JA024861
621
622 Kil, H., W. K. Lee, J. Shim, L. J. Paxton, and Y. Zhang (2013), The effect of the 135.6nm
623 emission originated from the ionosphere on the TIMED/GUVI O/N_2 ratio, J. Geophys. Res.
624 Space Physics, 118, 859–865, doi:10.1029/2012JA018112.
625
626 Kil, H., and L. J. Paxton (2011), The origin of the nonmigrating tidal structure in the column
627 number density ratio of atomic oxygen to molecular nitrogen, Geophys. Res. Lett., 38, L19108,
628 doi:10.1029/2011GL049432.
629
630 Maute, A., 2017. Thermosphere-Ionosphere-Electrodynamics General Circulation Model for the
631 Ionospheric Connection Explorer: TIEGCM-ICON. Space Science Reviews, 212(1-2), pp.523-
632 551. DOI: 10.1007/s11214-017-0330-3

633

634 Meier R. R., et al. (2015) Remote Sensing of Earth's Limb by TIMED/GUVI: Retrieval of
635 thermospheric composition and temperature, Earth and Space Science, 2, 1–37, doi: 10.1002/
636 2014EA000035.

637

638 Meier, R. R. (2021). The thermospheric column O/N2 ratio. *Journal of Geophysical Research:*
639 *Space Physics*, *126*, e2020JA029059. https://doi. org/10.1029/2020JA029059

640

641 Mende, S.B., H.U. Frey, K. Rider, C. Chou, S.E. Harris, O.H.W. Siegmund, S.L. England, C.W.
642 Wilkins, W.W. Craig, P. Turin, N. Darling, T.J. Immel, J. Loicq, P. Blain, E. Syrstadt, B.
643 Thompson, R. Burt, J. Champagne, P. Sevilla, S. Ellis (2017), The far ultra-violet imager on the
644 ICON mission. Space Sci. Rev. https://doi.org/10.1007/s11214-ß017-0386-0

645

646 Nicholas, A. C., Craven, J. D., and Frank, L. A. (1997), A survey of large-scale variations in
647 thermospheric oxygen column density with magnetic activity as inferred from observations of
648 the FUV dayglow, *J. Geophys. Res.*, 102(A3), 4493–4510, doi:10.1029/96JA03464.

649

650 Oberheide, J., and J. M. Forbes (2008), Tidal propagation of deep tropical cloud signatures into
651 the thermosphere from TIMED observations, Geophys. Res. Lett., 35, L04816,
652 doi:10.1029/2007GL032397.

653

Oberheide, J., Pedatella, N. M., Gan, Q., Kumari, K., Burns, A. G., & Eastes, R. (2020). Thermospheric composition O/N2 response to an altered meridional mean circulation during Sudden Stratospheric Warmings observed by GOLD. *Geophysical Research Letters*, 47, e2019GL086313. https://doi.org/10.1029/2019GL086313

Picone, J.M., A.E. Hedin, D.P. Drob, and A.C. Aikin, (2002) NRLMSISE-00 empirical model of the atmosphere: Statistical comparisons and scientific issues, J. Geophys. Res., 107(A12), 1468, doi:10.1029/2002JA009430

Sagawa, E., T.J. Immel, H.U. Frey, S.B. Mende, Longitudinal structure of the equatorial anomaly in the nighttime ionosphere observed by IMAGE/FUV. J. Geophys. Res. 110, 11302 (2005)

Schunk, R.W., (1983) The terrestrial ionosphere, in Solar-Terrestrial Physics (R.L. Carovillano and J.M. Forbes, eds.), 609, Reidel Publ. Co., Dordrecht.

Shepherd, G. G. (2011), Thermospheric observations of equatorial wavenumber 4 density perturbations from WINDII data, Geophys. Res. Lett., 38, L08801, doi:10.1029/2011GL046986.

Sirk, M. M., Korpela, E. J., Ishikawa, Y., Edelstein, J., Wishnow, E. H., Smith, C., McCauley J., McPhate J.B., Curtis J., and Gibson, S. R., 2017. Design and performance of the ICON EUV spectrograph. Space Science Reviews, 212(1-2), pp.631-643. DOI: 10.1007/s11214-017-0384-2

677 Stephan, A. W., Finn, S. C., Cook, T. A., Geddes, G., Chakrabarti, S., & Budzien, S. A. (2019).
678 Imaging of the daytime ionospheric equatorial arcs with extreme and far ultraviolet airglow.
679 *Journal of Geophysical Research: Space Physics*, *124*. https://doi.org/10.1029/2019JA026624
680
681 Stephan, A.W., Korpela, E.J., Sirk, M.M., England, S.L. and Immel, T.J., (2017). Daytime
682 Ionosphere Retrieval Algorithm for the Ionospheric Connection Explorer (ICON). Space Science
683 Reviews, 212(1-2), pp.645-654 DOI: 10.1007/s11214-017-0385-1
684
685 Stephan, A. W., Meier, R. R., England, S. L., Mende, S. B., Frey, H. U. and Immel, T. J., (2018).
686 Daytime O/N_2 Retrieval Algorithm for the Ionospheric Connection Explorer (ICON). Space
687 Science Reviews, DOI: 10.1007/s11214-018-0477-6
688
689 Stevens, M.H., Englert, C.R., Harlander, J.M., England, S.L., Marr, K.D., Brown, C.M., and
690 Immel, T.J., (2018). Retrieval of Lower Thermospheric Temperatures from O_2 A Band Emission
691 The MIGHTI Experiment on ICON, Space Science Reviews, 214: 4.
692 https://doi.org/10.1007/s11214-017-0434-9
693
694 Strickland, D. J., Cox, R. J., Meier, R. R., and Drob, D. P. (1999), Global O/N2 derived from DE
695 1 FUV dayglow data: Technique and examples from two storm periods", J. Geophys. Res., vol.
696 104, no. A3, pp. 4251–4266, 1999. doi:10.1029/98JA02817.
697
698 Strickland, D. J., J. S. Evans, and L. J. Paxton (1995), Satellite remote sensing of thermospheric
699 O/N_2 and solar EUV, 1, Theory, *J. Geophys. Res.*, *100*, 12,217.

Torr MR, Torr D. (1985). Ionization frequencies for solar cycle 21: revised. *J Geophys Res: Space Phys* 90 (A7): 6675–6678. https://doi.org/10.1029/JA090iA07p06675.

Zhang, Y., L. J. Paxton, D. Morrison, B. Wolven, H. Kil, C.-I. Meng, S. B. Mende, and T. J. Immel (2004), O/N2 changes during 1–4 October 2002 storms: IMAGE SI-13 and TIMED/GUVI observations, J. Geophys. Res., 109, A10308, doi:10.1029/2004JA010441.

Zhang, S. P., and G. G. Shepherd (2005), On the response of the O(^{1}S) dayglow emission rate to the Sun's energy input: An empirical model deduced from WINDII/UARS global measurements, J. Geophys. Res., 110, A03304, doi:10.1029/2004JA010887.

Zhang, Y., S. England, and L. J. Paxton (2010), Thermospheric composition variations due to nonmigrating tides and their effect on ionosphere, Geophys. Res. Lett., 37, L17103, doi:10.1029/2010GL044313.

Figure 11 Observed sub-limb FUV SW and LW airglow brightness for March 15, 2020. Panel a shows the brightness of the two airglow features as a function of local time. Panel b shows the brightness of the two airglow features as a function of solar zenith angle. In Panels a and b, the yellow points correspond to the SW airglow passband and the blue points correspond to the LW airglow passband. Panel c shows the location of the observed points, as a function of latitude and local time. Panel d shows the location of the observed points, as a function of latitude and solar zenith angle.

Figure 12 Brightness of the SW and LW airglow and their ratio for days 1 – 45 of 2020. Panel a shows the brightness of the SW airglow as a function of latitude and local time. Panel b shows the brightness of the LW airglow as a function of latitude and local time. Panel c shows the ratio of the brightness of the SW to the brightness of the LW airglow as a function of latitude and local time.

Figure 13 Retrieved $\Sigma O/N_2$ compared to the MSIS model. Panel a shows the location of the observations on January 2, 2020 as a function of latitude and solar zenith angle. Panel b shows the retrieved $\Sigma O/N_2$ from ICON and the MSIS model for each point observed during January 2, 2020, as a function of solar zenith angle. Panel c shows the one standard deviation uncertainty in each of the retrieved $\Sigma O/N_2$ from ICON for each point observed during January 2, 2020, as a function of solar zenith angle. Panel d shows the ratio between the retrieved $\Sigma O/N_2$ from ICON and the MSIS model for each observation made during the first 6 months of 2020, as a function

of local time. The purple dots represent the value for each observation. The green lines show the mean and standard deviation of these points at each 1-hour interval, and the orange line show the range from the 5th to the 95th percentile points at each 1-hour interval. The average ratio between ICON and MSIS is 0.84 and the average of the standard deviations is 0.089.

Figure 14 geographic variation in the $\Sigma O/N_2$ from ICON and MSIS. Panels a, c and e show the ICON values and panels b, d, and f show the MSIS values. Panels a and b are for days 1 – 45, 2020. Panels c and d are for days 46 – 90, 2020. Panels e and f are for days 136 – 180, 2020. All values are from 11 – 13 hours local time. Note the different color scales used for the ICON and MSIS values, such that the variations with latitude and season are visible. Note that data are available in the southern hemisphere near 300 degrees longitude as these remote observation locations correspond to when the ICON spacecraft is within the South Atlantic Anomaly.

Figure 15 Amplitude of the DE3 and SE2 non-migrating tides observed by MIGHTI at 97 km altitude during the first 100 days of 2020. Panels a, c and e correspond to the DE3 tide and panels b, d and f correspond to the SE2 tide. Panels a and b show the temperature amplitude, panels c and d show the zonal wind amplitude and panels e and f correspond to the meridional wind amplitude. All values are shown at 97 km altitude, corresponding to the lower boundary of the TIEGCM model. Note the different scales used in each panel.

Figure 16 Wavenumber-4 component of the horizontal winds observed by MIGHTI as functions of longitude and local time. Panel a shows the zonal wind perturbation and panel b shows the meridional wind perturbation. All data represent the wavenumber-4 fit to the data that are averaged over days 75 – 100, 2020, altitudes from 150 – 160 km altitude and 25 – 35° north. The best-fit linear trend in the zonal wind (meridional wind) of 5.12° (7.00°)/ hour is shown with the black dotted lines.

Figure 17 Wavenumber-4 component of the perturbation in the $\Sigma O/N_2$ retrieved from the ICON observations as functions of day of year, local time and longitude. Panel a shows the data from the ascending portion of the orbit and panel b shows the data from the descending portion of the orbit. All data are averaged over 25 – 35° north. The amplitude of the $\Sigma O/N_2$ perturbation is determined relative to the mean value at each day of year (corresponding to a single local time). The solid line shown in panel b indicates the phase shift with local time expected for the DE3 tide and is included as a visual guide.

Figure 18 Wavenumber-4 perturbation in the neutral winds and $\Sigma O/N_2$ ratios from the TIEGCM model as functions of local time and longitude. Values are averaged over 25 to 35° north and over days 75 – 95 of 2020. Panels a – c show the perturbation in the zonal, meridional and vertical wind respectively. The horizontal winds are shown in m/s and the vertical wind is shown in cm/s. Panel d shows the perturbation to the $\Sigma O/N_2$ and is expressed as a percentage of the

zonal mean value at each local time. The dashed black line shows a phase shift of 3.75° / hour as would be expected from a DE3 tide.

Figure 19 Wavenumber-4 component of the pertrubation in ionospheric nmF2 and column O^+ abundance retrieved from ICON EUV observations as functions of day of year and longitude. Panel a shows the perturbation in the total column O^+ and panel b shows the perturbation in the NmF2 value. All data are from the descending portion of the orbit and are averaged over 25 – 35° north.

Figure 20 Wavenumber-4 perturbation of the 557.7 nm airglow observed by MIGHTI Channel A as a function of local time and longitude. All data are averaged over days 75 – 100, 2020, tangent altitudes from 150 – 160 km altitude and 25 – 35° north. All values are expressed as a percent of the zonal mean value.

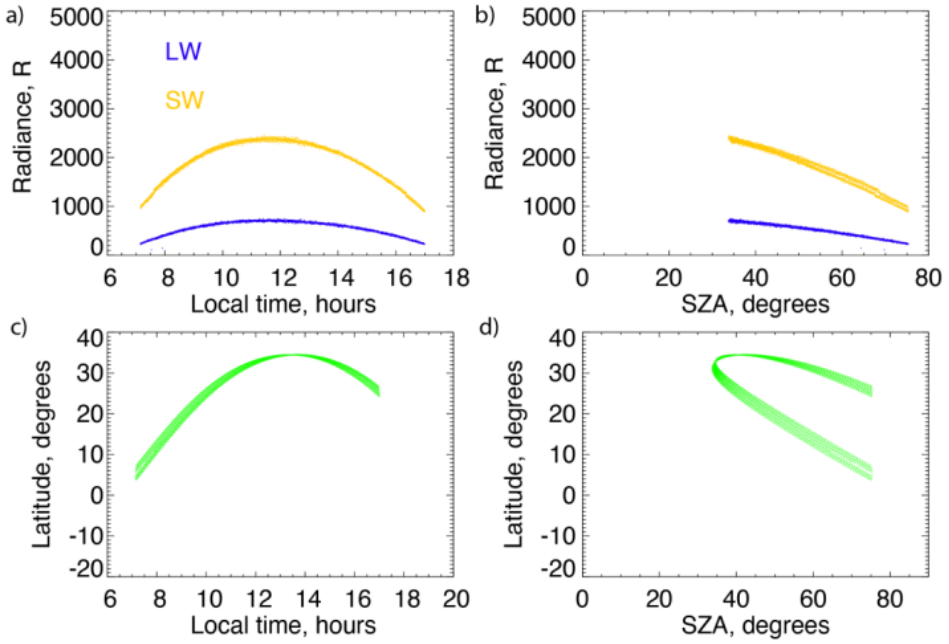
a)
b)
c)
d)
LW
SW
Radiance, R
Local time, hours
SZA, degrees
Latitude, degrees

800

801

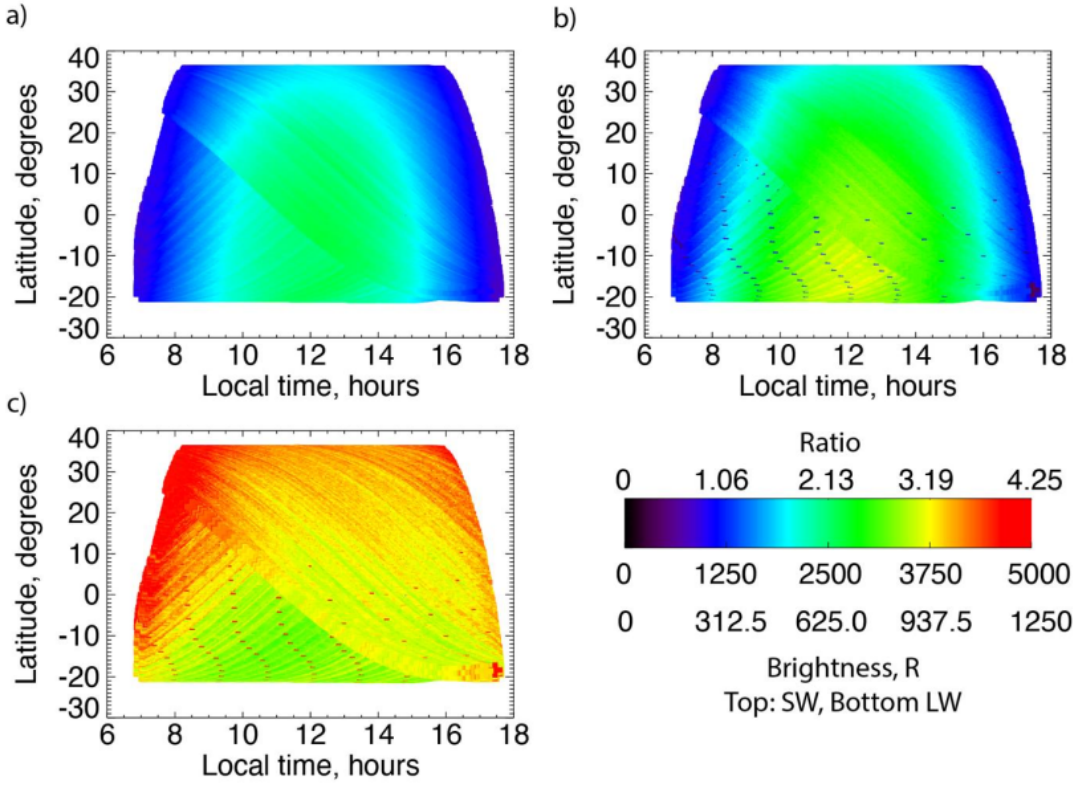
a)
b)
c)
Latitude, degrees
Local time, hours
Ratio
0
1.06
2.13
3.19
4.25
0
1250
2500
3750
5000
0
312.5
625.0
937.5
1250
Brightness, R
Top: SW, Bottom LW

802

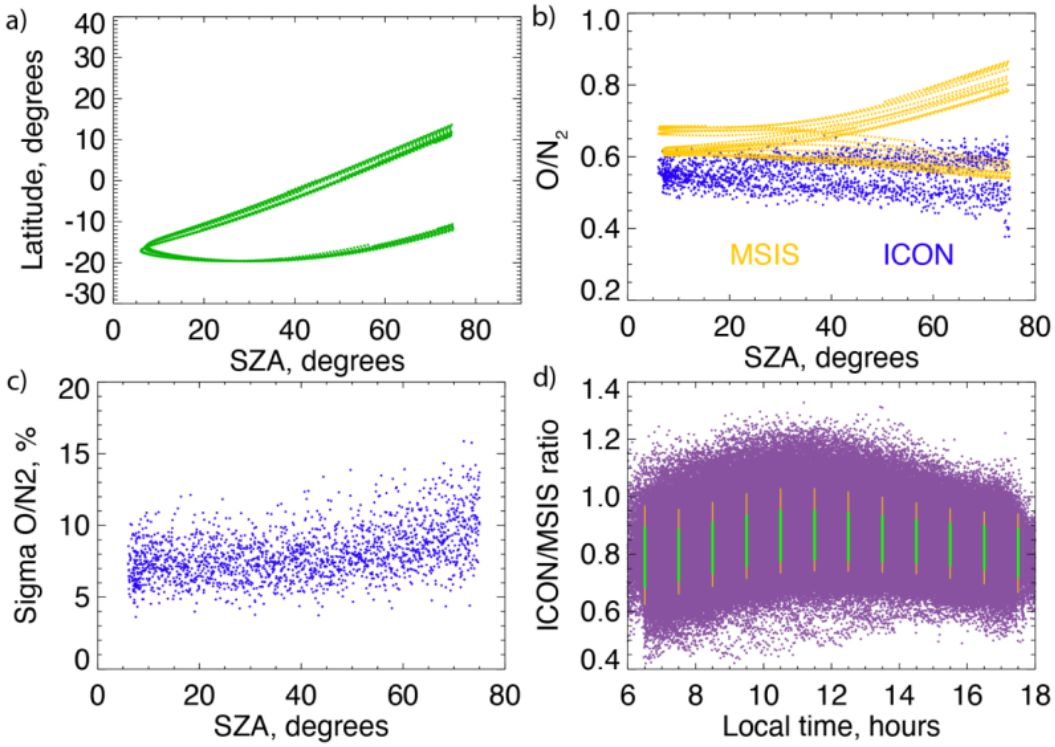
a)
Latitude, degrees
SZA, degrees
b)
O/N2
MSIS
ICON
SZA, degrees
c)
Sigma O/N2, %
SZA, degrees
d)
ICON/MSIS ratio
Local time, hours

803

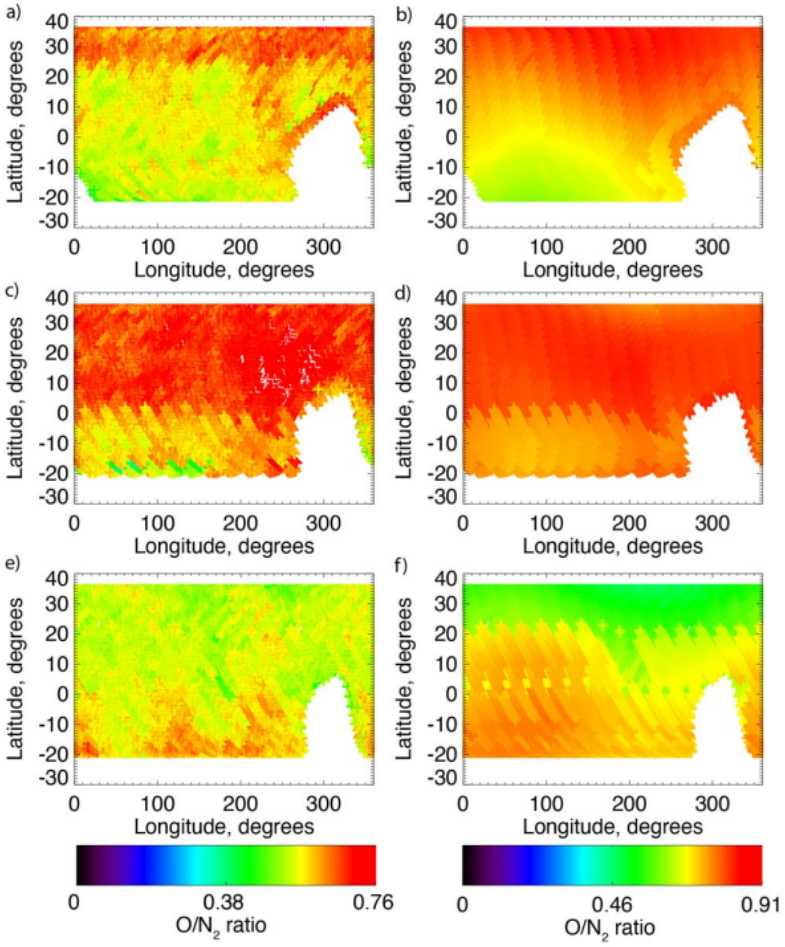
a)
b)
c)
d)
e)
f)
Latitude, degrees
Longitude, degrees
40
30
20
10
0
-10
-20
-30
0
100
200
300
0
0.38
0.76
O/N2 ratio
0
0.46
0.91
O/N2 ratio

804

805

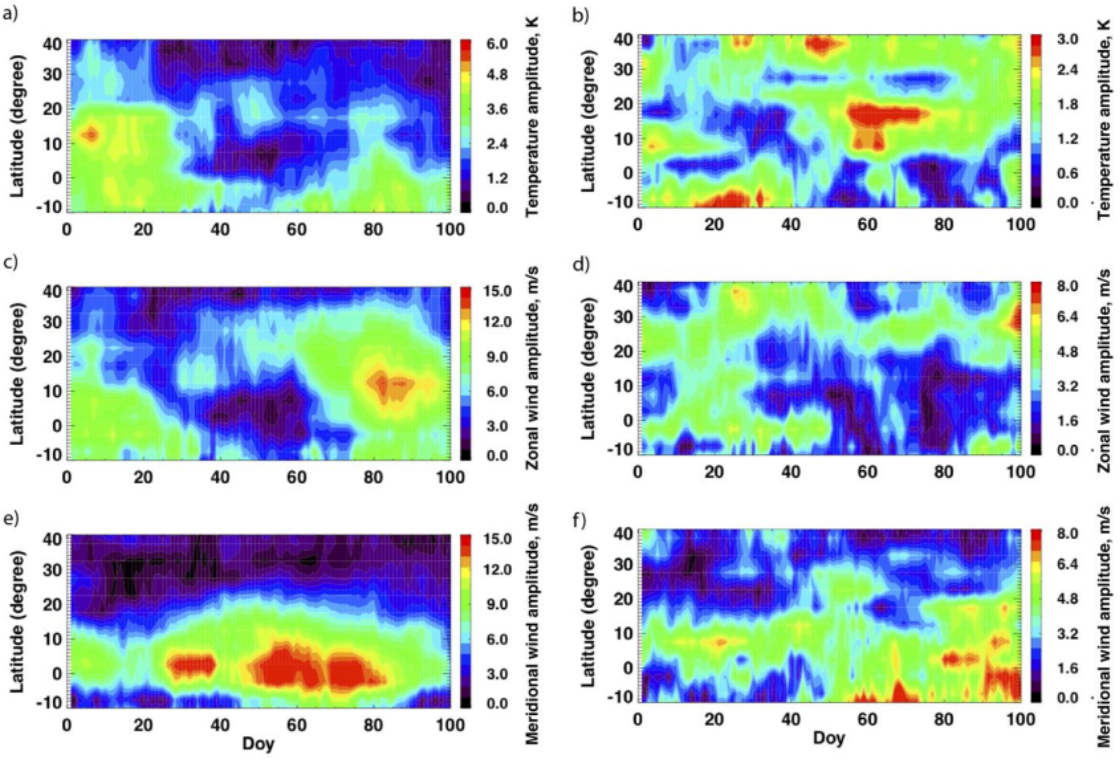
a)
b)
c)
d)
e)
f)
Latitude (degree)
Doy
Temperature amplitude, K
Zonal wind amplitude, m/s
Meridional wind amplitude, m/s

806

807

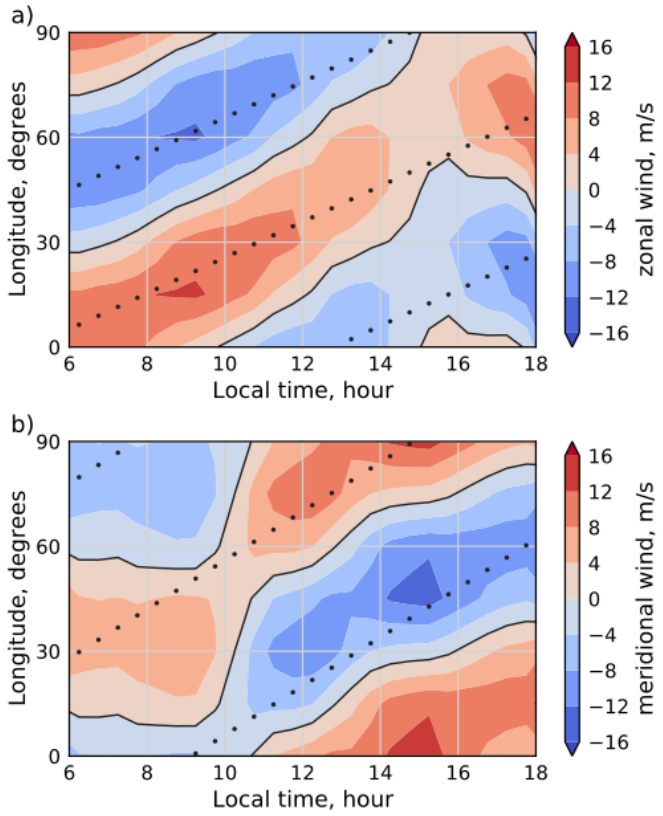

808

809

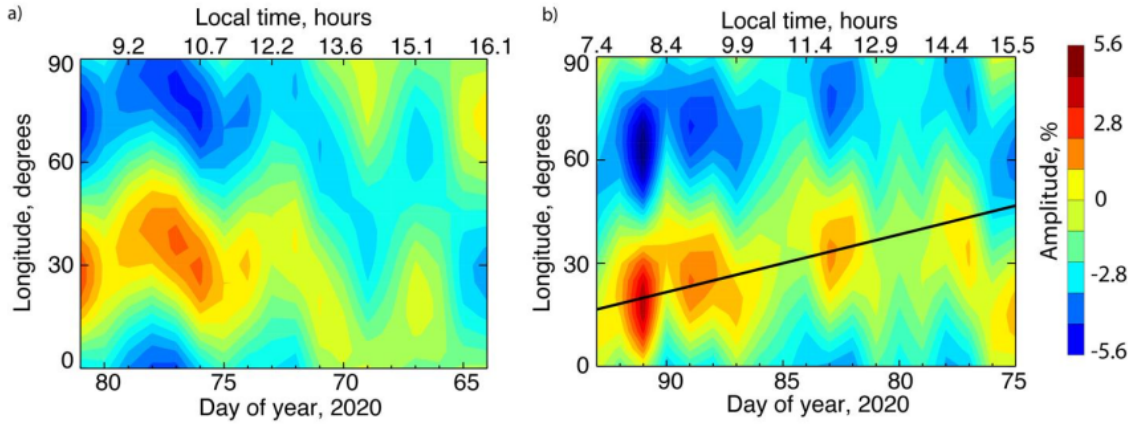

810

811

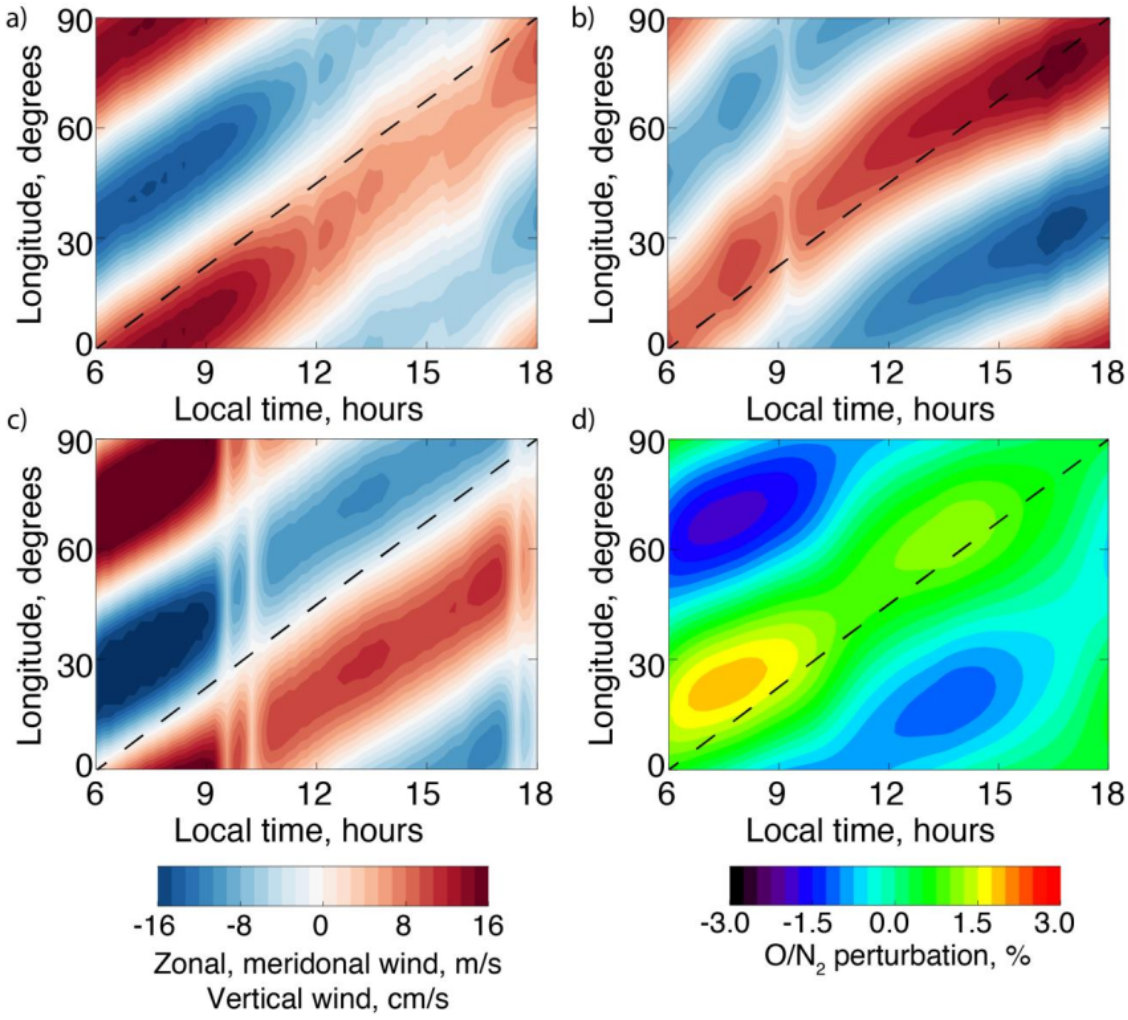
a)
b)
c)
d)
Longitude, degrees
Local time, hours
0
30
60
90
6
9
12
15
18
-16
-8
0
8
16
Zonal, meridonal wind, m/s
Vertical wind, cm/s
-3.0
-1.5
0.0
1.5
3.0
O/N2 perturbation, %

812

813

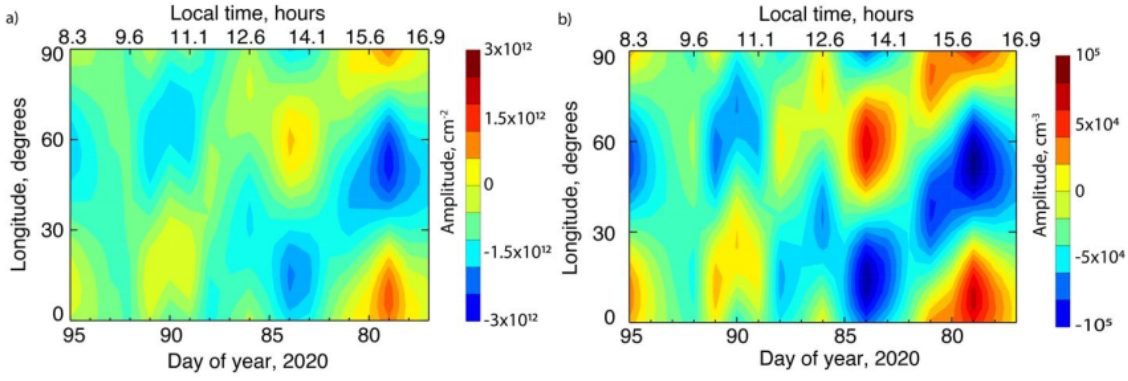
a)
b)
Local time, hours
8.3
9.6
11.1
12.6
14.1
15.6
16.9
Longitude, degrees
0
30
60
90
Day of year, 2020
95
90
85
80
Amplitude, cm-2
3x10¹²
1.5x10¹²
0
-1.5x10¹²
-3x10¹²
Amplitude, cm-3
10⁵
5x10⁴
0
-5x10⁴
-10⁵

814

815

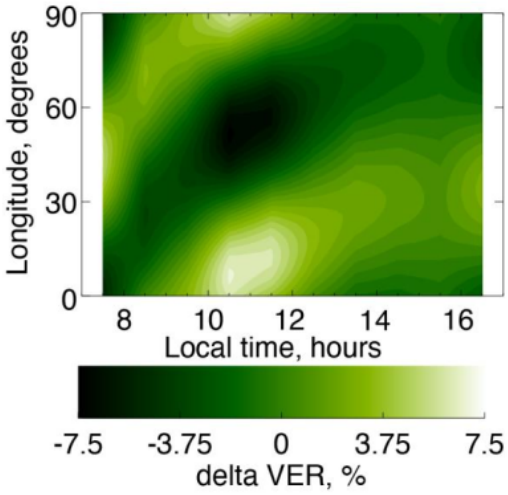
90
60
30
0
Longitude, degrees
8
10
12
14
16
Local time, hours
-7.5
-3.75
0
3.75
7.5
delta VER, %

816

First results from the retrieved column O/N2 ratio from the Ionospheric Connection Explorer (ICON): Longitudinal structures induced by nonmigrating tides

ORIGINALITY REPORT

14%
SIMILARITY INDEX

PRIMARY SOURCES

1	S. L. England, G. Liu, E. Yiğit, P. R. Mahaffy, M. Elrod, M. Benna, H. Nakagawa, N. Terada, B. Jakosky. "MAVEN NGIMS observations of atmospheric gravity waves in the Martian thermosphere", Journal of Geophysical Research: Space Physics, 2017 Crossref	102 words — 1%
2	Scott L. England, Katelynn R. Greer, Shun‐Rong Zhang, Scott Evans et al. "First comparison of travelling atmospheric disturbances observed in the middle thermosphere by GOLD to travelling ionospheric disturbances seen in ground‐based total electron content observations", Journal of Geophysical Research: Space Physics, 2021 Crossref	100 words — 1%
3	link.springer.com Internet	89 words — 1%
4	England, Scott L., Guiping Liu, Paul Withers, Erdal Yiğit, Daniel Lo, Sonal Jain, Nicholas M. Schneider, Justin Deighan, William E. McClintock, Paul R. Mahaffy, Meredith Elrod, Mehdi Benna, and Bruce M. Jakosky. "Simultaneous observations of atmospheric tides from combined in situ and remote observations at Mars from the MAVEN spacecraft : In	67 words — 1%

situ and remote observations of tides", Journal of Geophysical Research Planets, 2016.
Crossref

5 Pedatella, N. M.. "Observations and simulations of the ionospheric lunar tide: Seasonal variability", Journal of Geophysical Research Space Physics, 2014.
Crossref
48 words — 1%

6 agupubs.pericles-prod.literatumonline.com
Internet
47 words — 1%

7 agupubs.onlinelibrary.wiley.com
Internet
37 words — < 1%

8 Trong Bui, Brett Pipitone, Keith Krake. "In-Flight Capability for Evaluating Skin-Friction Gages and Other Near-Wall Flow Sensors", 41st Aerospace Sciences Meeting and Exhibit, 2003
Crossref
32 words — < 1%

9 Scott L. England, Katelynn R. Greer, Stanley C. Solomon, Richard W. Eastes, William E. McClintock, Alan G. Burns. "Observation of thermospheric gravity waves in the Southern Hemisphere with GOLD", Journal of Geophysical Research: Space Physics, 2020
Crossref
31 words — < 1%

10 Larry J. Paxton, Yongliang Zhang, Hyosub Kil, Robert K. Schaefer. "Exploring the Upper Atmosphere", Wiley, 2021
Crossref
30 words — < 1%

11 Sato, K.. "A statistical study of the structure, saturation and sources of inertio-gravity waves in the lower stratosphere observed with the MU radar", Journal of Atmospheric and Terrestrial Physics, 199405
Crossref
28 words — < 1%

12	Scott L. England, Guiping Liu, Aishwarya Kumar, Paul R. Mahaffy et al. "Atmospheric Tides at High Latitudes in the Martian Upper Atmosphere Observed by MAVEN and MRO", Journal of Geophysical Research: Space Physics, 2019 Crossref	26 words — < 1%
13	angeo.copernicus.org Internet	26 words — < 1%
14	Y. Kakinami. "Empirical models of Total Electron Content based on functional fitting over Taiwan during geomagnetic quiet condition", Annales Geophysicae, 08/26/2009 Crossref	25 words — < 1%
15	worldwidescience.org Internet	25 words — < 1%
16	hdl.handle.net Internet	24 words — < 1%
17	Häusler, K., M. E. Hagan, J. M. Forbes, X. Zhang, E. Doornbos, S. Bruinsma, and G. Lu. "Intra-annual variability of tides in the thermosphere from model simulations and in-situ satellite observations : Intra-annual tidal variability", Journal of Geophysical Research Space Physics, 2014. Crossref	22 words — < 1%
18	progearthplanetsci.springeropen.com Internet	21 words — < 1%
19	Brian J. Harding, Jorge L. Chau, Maosheng He, Christoph R. Englert et al. "Validation of ICON - MIGHTI thermospheric wind observations: 2. Green - line	18 words — < 1%

comparisons to specular meteor radars", Journal of Geophysical Research: Space Physics, 2021
Crossref

20	www.ann-geophys.net Internet	18 words — < 1%
21	www.swsc-journal.org Internet	18 words — < 1%
22	R. A. Heelis, R. A. Stoneback, M. D. Perdue, M. D. Depew et al. "Ion Velocity Measurements for the Ionospheric Connections Explorer", Space Science Reviews, 2017 Crossref	17 words — < 1%
23	Cornelius Csar Jude H. Salinas, Loren C. Chang, Mao - Chang Liang, Jia Yue et al. " Local - Time Variabilities of March Equinox Daytime SABER CO in the Upper Mesosphere and Lower Thermosphere Region ", Journal of Geophysical Research: Space Physics, 2020 Crossref	16 words — < 1%
24	N. M. Pedatella. "Day-to-day migrating and nonmigrating tidal variability due to the six-day planetary wave", Journal of Geophysical Research, 06/01/2012 Crossref	16 words — < 1%
25	docplayer.net Internet	16 words — < 1%
26	sprg.ssl.berkeley.edu Internet	16 words — < 1%
27	www.nrcresearchpress.com Internet	16 words — < 1%

28 "Modeling the Ionosphere-Thermosphere System", Wiley, 2014 — 15 words — < 1%
Crossref

29 Brian J. Harding, Jorge L. Chau, Maosheng He, Christoph R. Englert et al. "Validation of ICON - MIGHTI Thermospheric Wind Observations: 2. Green - Line Comparisons to Specular Meteor Radars", Journal of Geophysical Research: Space Physics, 2021 — 15 words — < 1%
Crossref

30 Christoph R. Englert, John Mark Harlander, Charles M. Brown, Andrew W. Stephan et al. "The Michelson Interferometer for Global High-resolution Thermospheric Imaging (MIGHTI): Wind and Temperature Observations from the Ionospheric Connection Explorer (ICON)", Imaging and Applied Optics, 2013 — 15 words — < 1%
Crossref

31 Murray R. Horne, Gerard M. Martin, Carolyn W. Harley, Darlene M. Skinner. "Where am I? Distal cues use requires sensitivity to start location change in the rat.", Journal of Experimental Psychology: Animal Behavior Processes, 2007 — 14 words — < 1%
Crossref

32 E. M. B. Thiemann, M. Dominique, M. D. Pilinski, F. G. Eparvier. "Vertical Thermospheric Density Profiles From EUV Solar Occultations Made by PROBA2 LYRA for Solar Cycle 24", Space Weather, 2017 — 13 words — < 1%
Crossref

33 S. L. England. "Modeling of multiple effects of atmospheric tides on the ionosphere: An examination of possible coupling mechanisms responsible for — 12 words — < 1%

the longitudinal structure of the equatorial ionosphere", Journal of Geophysical Research, 05/25/2010
Crossref

34 Zhang, F.. "Microscale isolation and analysis of heparin from plasma using an anion-exchange spin column", Analytical Biochemistry, 20060615 — 12 words — < 1%
Crossref

35 Cho, Young-Min, and Gordon Shepherd. "Resolving daily wave 4 non-migrating tidal winds at equatorial and mid latitudes with WINDII: DE3 and SE2 : Wave 4 Non-Migrating Tides: DE3 and SE2", Journal of Geophysical Research Space Physics, 2015. — 11 words — < 1%
Crossref

36 epdf.pub — 11 words — < 1%
Internet

37 Gordon G. Shepherd. "Global thermospheric atomic oxygen variations observed with the WIND Imaging Interferometer (WINDII): Wave 4 at low and high latitudes", Journal of Geophysical Research, 10/18/2011 — 10 words — < 1%
Crossref

38 Torr, D.G.. "Chemistry of the thermosphere and ionosphere", Journal of Atmospheric and Terrestrial Physics, 197907/08 — 10 words — < 1%
Crossref

39 J. M. Forbes. "Troposphere-thermosphere tidal coupling as measured by the SABER instrument on TIMED during July–September 2002", Journal of Geophysical Research, 2006 — 9 words — < 1%
Crossref

40 K. Shiokawa. "Low-latitude auroras observed in Japan: 1999–2004", Journal of Geophysical — 9 words — < 1%

Research, 2005
Crossref

41 R. Pfaff. "Observations of DC electric fields in the low-latitude ionosphere and their variations with local time, longitude, and plasma density during extreme solar minimum", Journal of Geophysical Research, 12/21/2010 — 9 words — < 1%
Crossref

42 R. R. Meier. " The thermospheric column O/N ratio ", Journal of Geophysical Research: Space Physics, 2021 — 9 words — < 1%
Crossref

43 Yongliang Zhang. "Thermospheric composition variations due to nonmigrating tides and their effect on ionosphere", Geophysical Research Letters, 09/14/2010 — 9 words — < 1%
Crossref

44 mtc-m21b.sid.inpe.br — 9 words — < 1%
Internet

45 science.nasa.gov — 9 words — < 1%
Internet

46 "Climate and Weather of the Sun-Earth System (CAWSES)", Springer Science and Business Media LLC, 2013 — 8 words — < 1%
Crossref

47 "Magnetospheric Imaging — The Image Prime Mission", Springer Science and Business Media LLC, 2003 — 8 words — < 1%
Crossref

48 C. H. Chen, C. H. Lin, T. Matsuo, W. H. Chen, I. T. Lee, J. Y. Liu, J. T. Lin, C. T. Hsu. "Ionospheric data — 8 words — < 1%

assimilation with thermosphere-ionosphere-electrodynamics general circulation model and GPS-TEC during geomagnetic storm conditions", Journal of Geophysical Research: Space Physics, 2016
Crossref

49 D. V. Bisikalo. "Remote sensing of the proton aurora characteristics from IMAGE-FUV", Annales Geophysicae, 2003 — 8 words — < 1%
Crossref

50 Endawoke Yizengaw. "Global Longitudinal Dependence Observation of the Neutral Wind and Ionospheric Density Distribution", International Journal of Geophysics, 2012 — 8 words — < 1%
Crossref

51 Federico Gasperini, Maura E. Hagan, Jeffrey M Forbes. "Seminal Evidence of a 2.5-sol Ultra-Fast Kelvin Wave in Mars' Middle and Upper Atmosphere", Geophysical Research Letters, 2018 — 8 words — < 1%
Crossref

52 Guiping Liu, Ruth S. Lieberman, V. Lynn Harvey, Nicholas M. Pedatella et al. "Tidal Variations in the Mesosphere and Lower Thermosphere Before, During, and After the 2009 Sudden Stratospheric Warming", Journal of Geophysical Research: Space Physics, 2021 — 8 words — < 1%
Crossref

53 J. S. Evans, J. D. Lumpe, J. Correira, V. Veibell, A. Kyrwonos, W. E. McClintock, S. C. Solomon, R. W. Eastes. "Neutral Exospheric Temperatures From the GOLD Mission", Journal of Geophysical Research: Space Physics, 2020 — 8 words — < 1%
Crossref

54 Pedatella, N. M., and H.-L. Liu. "Influence of the El Niño Southern Oscillation on the middle and upper — 8 words — < 1%

atmosphere : ENSO TIDAL VARIABILITY", Journal of Geophysical Research Space Physics, 2013.
Crossref

55	acd.ucar.edu Internet	8 words — < 1%
56	apps.dtic.mil Internet	8 words — < 1%
57	journals.sagepub.com Internet	8 words — < 1%
58	mafiadoc.com Internet	8 words — < 1%
59	R. R. Meier, J. M. Picone, D. Drob, J. Bishop et al. "Remote Sensing of Earth's Limb by TIMED/GUVI: Retrieval of thermospheric composition and temperature", Earth and Space Science, 2015 Crossref	7 words — < 1%
60	Shepherd, Marianna G., Gordon G. Shepherd, and Young-Min Cho. "Longitudinal variability of thermospheric temperatures from WINDII O(¹S) dayglow", Journal of Geophysical Research, 2012. Crossref	7 words — < 1%
61	Astrid Maute. "Thermosphere-Ionosphere-Electrodynamics General Circulation Model for the Ionospheric Connection Explorer: TIEGCM-ICON", Space Science Reviews, 2017 Crossref	6 words — < 1%
62	GuangXing Ding, Bo Chen, XiaoXin Zhang, Fei He. "A method to derive global O/N2 ratios from	6 words — < 1%

SSUSI/DMSP based on Re-AURIC algorithm", Journal of Atmospheric and Solar-Terrestrial Physics, 2020
Crossref

63 John M. Harlander, Christoph R. Englert. "Laboratory demonstration of mini-MIGHTI: A prototype sensor for thermospheric red-line (630 nm) neutral wind measurements from a 6U CubeSat", Journal of Atmospheric and Solar-Terrestrial Physics, 2020 — 6 words — < 1%
Crossref

64 R. R. Meier. " The Thermospheric Column O/N Ratio ", Journal of Geophysical Research: Space Physics, 2021 — 6 words — < 1%
Crossref

65 S. Tulasi Ram. "FORMOSAT-3/COSMIC observations of seasonal and longitudinal variations of equatorial ionization anomaly and its interhemispheric asymmetry during the solar minimum period", Journal of Geophysical Research, 06/19/2009 — 6 words — < 1%
Crossref

66 Shepherd, Gordon G., Raymond G. Roble, and Young-Min Cho. "WINDII observations and TIME-GCM simulations of O(1 S) polar spirals during geomagnetic disturbances : POLAR SPIRALS DURING GEOMAGNETIC EVENTS", Journal of Geophysical Research Space Physics, 2013. — 6 words — < 1%
Crossref

67 Wang, Sicheng, Sixun Huang, and Hanxian Fang. "Wave-3 and wave-4 patterns in the low- and mid-latitude ionospheric TEC", Journal of Atmospheric and Solar-Terrestrial Physics, 2015. — 6 words — < 1%
Crossref

EXCLUDE QUOTES	ON	EXCLUDE MATCHES	OFF
EXCLUDE BIBLIOGRAPHY	ON		